

# Radar in non-destructive testing of thin granular dielectric layers

---

Eeva Huuskonen-Snicker

# Radar in non-destructive testing of thin granular dielectric layers

**Eeva Huuskonen-Snicker**

A doctoral dissertation completed for the degree of Doctor of Science (Technology) to be defended, with the permission of the Aalto University School of Engineering, at a public examination held at the lecture hall R1 of the school on 27 January 2017 at 12.

**Aalto University  
School of Engineering  
Department of Civil Engineering**

**Supervising professor**

Professor Jussi Leveinen, Aalto University, Finland

**Thesis advisor**

Professor Terhi Pellinen, Aalto University, Finland

**Preliminary examiners**

Professor Hermann Rohling, Technische Universität Hamburg-Harburg, Germany

Professor Ari Visa, Tampere University of Technology, Finland

**Opponent**

Dr. Jukka Ruoskanen, Finnish Defense Research Agency, Finland

Aalto University publication series

**DOCTORAL DISSERTATIONS** 279/2016

© Eeva Huuskonen-Snicker

ISBN 978-952-60-7229-6 (printed)

ISBN 978-952-60-7228-9 (pdf)

ISSN-L 1799-4934

ISSN 1799-4934 (printed)

ISSN 1799-4942 (pdf)

<http://urn.fi/URN:ISBN:978-952-60-7228-9>

Unigrafia Oy

Helsinki 2016

Finland

**Author**

Eeva Huuskonen-Snicker

**Name of the doctoral dissertation**

Radar in non-destructive testing of thin granular dielectric layers

**Publisher** School of Engineering

**Unit** Department of Civil Engineering

**Series** Aalto University publication series DOCTORAL DISSERTATIONS 279/2016

**Field of research** Engineering Geology

**Manuscript submitted** 25 October 2016

**Date of the defence** 27 January 2017

**Permission to publish granted (date)** 29 November 2016

**Language** English

☒ **Monograph**

☐ **Article dissertation**

☐ **Essay dissertation**

**Abstract**

Ground-penetrating radar (GPR) is an electromagnetic probing and imaging method of subsurface which is applied in the non-destructive evaluation of roads and bridges as well. In Finland, the GPR is a commonly used quality control method for the air void content of newly laid asphalt pavements. The air void content has an effect on the long-term performance of the pavement. The GPR method is based on deriving the relative permittivity, or dielectric constant, from the reflected radar signal. The air void content is then estimated from the relative permittivity based on the drilled calibration asphalt core. One of the problems related to the current GPR method is the insufficient depth resolution of conventional, 1-2 GHz systems.

The objective of this study was to analyse if GPR, or microwave technology in general, can be applied in the air void content assessment of thin asphalt layers. Furthermore, this study aims to provide an understanding about factors affecting the relative permittivity measurements of heterogeneous, granular and layered media. A 12-18 GHz microwave radar with centimetre scale depth resolution was developed for studying thin asphalt layers. Unfortunately, the necessary solution of increasing the centre frequency produced other problems due to the asphalt granularity. The largest aggregate grains in asphalt are about the same size as the wavelength at employed frequencies. Different laboratory tests were conducted for better understanding the relative permittivity variations of pavements. Resonator based surveys included both the magnetic permeability and relative permittivity measurements of rock specimens. Most of the laboratory studies were free space measurements with the vector network analyzer in the transmission configuration at the 7-17 GHz. Studied materials included asphalt raw materials, drilled asphalt samples and granulated plastic specimens.

The relative permittivity results of asphalt pavements and samples showed a wide range of values. It was concluded that the observed variation in permittivity does not simply result from changes in air void content. For example, the real part of the relative permittivity of the studied metavolcanic rock was 5.90-6.15, whereas the granular sample of the same rock type had values 3.17-8.12. Multiple reflections from individual granules can increase the observed permittivity of the studied mixture when the grain size is larger or of the order of the signal wavelength. The most of the permittivity variation is likely due to the mineralogical changes in rock aggregates, and changes in the volumetric portions of aggregates and bitumen in asphalt mix. Results of this study suggest that the current GPR method is not reliable in the air void content evaluation of thin pavement layers.

**Keywords** Radar, GPR, permittivity, asphalt, air voids

**ISBN (printed)** 978-952-60-7229-6

**ISBN (pdf)** 978-952-60-7228-9

**ISSN-L** 1799-4934

**ISSN (printed)** 1799-4934

**ISSN (pdf)** 1799-4942

**Location of publisher** Helsinki

**Location of printing** Helsinki

**Year** 2016

**Pages** 90

**urn** <http://urn.fi/URN:ISBN:978-952-60-7228-9>



**Tekijä**

Eeva Huuskonen-Snicker

**Väitöskirjan nimi**

Ohuiden rakeisten dielektristen kerrosten ainetta rikkomaton testaus tutkalla

**Julkaisija** Insinööritieteiden korkeakoulu**Yksikkö** Rakennustekniikan laitos**Sarja** Aalto University publication series DOCTORAL DISSERTATIONS 279/2016**Tutkimusala** Teknillinen geologia**Käsikirjoituksen pvm** 25.10.2016**Väitöspäivä** 27.01.2017**Julkaisuluvan myöntämispäivä** 29.11.2016**Kieli** Englanti☒ **Monografia**☐ **Artikkeliväitöskirja**☐ **Esseeväitöskirja****Tiivistelmä**

Maatutka on sähkömagneettinen maankamaran mittausta- ja luotausmenetelmä, jota sovelletaan myös teiden ja siltojen ainetta rikkomattomassa testauksessa. Suomessa maatutkaa käytetään yleisesti uusien asfalttipäällysteiden tyhjätilan laadunvalvonnassa. Tyhjätila on sidoksissa päällysteen pitkäaikaiseen kestävyys. Maatutkamenetelmä perustuu suhteellisen permittiivisyyden, tai dielektrisyysvakion, määrittämiseen heijastuneesta tutkasignaalista. Tämän jälkeen tyhjätila lasketaan suhteellisesta permittiivisyydestä asfaltista poratun kalibrointinäytteen avulla. Eräs nykyisen maatutkamenetelmän rajoituksista liittyy käytössä olevien 1-2 GHz:n maatutkalaitteistojen riittämättömyyden syvyysuuntaiseen erottelukykyn.

Tämän tutkimuksen tavoitteena oli selvittää voidaanko maatutkaa, tai mikroaaltotekniikkaa yleisemmin, käyttää ohuiden asfalttipäällysteiden tyhjätilan arviointiin. Lisäksi tavoitteena oli ymmärtää, mitkä tekijät vaikuttavat heterogeenisten rakeisten ja kerroksellisten materiaalien suhteellisen permittiivisyyden mittaukseen. Ohuiden asfalttipäällysteiden tutkimista varten kehitettiin 12-18 GHz:n mikroaaltotutka, jonka syvyysuuntaisen erottelukyky on senttimetrin luokkaa. Keskitäajuuden välttämättömyydestä korotuksesta seuraa valitettavasti ongelmia asfaltin rakeisuuden takia. Suurimmat yksittäiset kivet asfaltissa ovat samaa suuruusluokkaa kuin käytettyjä taajuuksia vastaava aallonpituus. Jotta päällysteistä mitattua suhteellisen permittiivisyyden hajontaa ymmärrettäisiin paremmin, laboratoriossa tehtiin erilaisia mittauksia. Resonaattorimittauksilla tutkittiin sekä kiviäytteen suhteellista permittiivisyyttä että magneettista permeabiliteettia. Suurin osa laboratoriokokeista oli vektoripiirianalysointia avulla tehtyjä läpäisymittauksia 7-17 GHz:llä. Tutkitut materiaalit sisälsivät asfaltin raaka-aineita, porattuja asfalttinäytteitä ja rakeisia muovinäytteitä.

Asfalttipäällysteistä ja -näytteistä mitatuilla suhteellisen permittiivisyyden arvoilla oli suuri vaihteluväli. Tutkimuksessa todettiin, että havaittu permittiivisyyden vaihtelu ei suoraan johdu tyhjätilan vaihteluista. Esimerkiksi tutkitun metavulkaniitti-kivilajin suhteellisen permittiivisyyden reaaliosa vaihteli 5,90-6,15, kun taas samasta kivilajista murskatun näytteen arvot olivat 3,17-8,12. Moninkertaiset heijastukset yksittäisistä rakeista voivat kasvattaa tutkitun seoksen havaittuja permittiivisyysarvoja, kun raekoko on suurempi tai aallonpituuden suuruusluokkaa. Suurin osa permittiivisyysvaihteluista on luultavasti seurausta kiviaineksen mineralogisista vaihteluista sekä kiviaineksen ja bitumin tilavuussuhteiden muutoksista asfaltista. Tutkimustulosten perusteella nykyinen maatutkamenetelmä ei ole luotettava ohuiden päällysteiden tyhjätilan arvioinnissa.

**Avainsanat** Tutka, maatutka, permittiivisyys, asfaltti, tyhjätila**ISBN (painettu)** 978-952-60-7229-6**ISBN (pdf)** 978-952-60-7228-9**ISSN-L** 1799-4934**ISSN (painettu)** 1799-4934**ISSN (pdf)** 1799-4942**Julkaisupaikka** Helsinki**Painopaikka** Helsinki**Vuosi** 2016**Sivumäärä** 90**urn** <http://urn.fi/URN:ISBN:978-952-60-7228-9>



# Acknowledgements

I can truly say that during my doctoral studies I have learned a great deal. What surprised me mostly, is not what I learned about science, but what I learned about working with different people. So, I wish to thank all the people who have helped, supported and encouraged me during this process. I thank my supervising Professor Jussi Leveinen for all comments he has made during these past six years. I also appreciate the instruction that I have received from Professor Terhi Pellinen. Working in different research projects during my doctoral studies has given me the privilege to work with many amazing people. I want to thank you all and, especially, Professor Pekka Eskelinen, late Professor Pertti Vainikainen, Dr. Valeri Mikhnev and doctoral students Martta-Kaisa Olkkonen and Ari Hartikainen, with whom I have had many inspiring discussions.

I am grateful for the funding that I have received for this thesis from the Finnish Transport Agency and the research project “Pavement Life Cycle Research Program, Assessment of Asphalt Pavement Density” in 2014-2015, from the Doctoral Programme in the Built Environment in 2010-2013, and from the Väisälä Foundation in 2016 for finalizing this thesis. I also appreciate the financial support from the Finnish Foundation for Technology Promotion (Tekniikan edistämissäätiö, TES), Confederation of Finnish Construction Industries (Rakennusteollisuus RT) and Finnish Pavement Technology Advisory Council (Päällystealan neuvottelukunta ry, PANK).

During these past six years, I moved to different offices many, many times but this has given me the opportunity to get to know wonderful people not only from Engineering Geology and Applied Geophysics research group at Aalto, but Rock Engineering and Highway Engineering at Aalto, as well as Geophysics department at Ludwig-Maximilians University in Munich, which I had the amazing opportunity to visit in 2010-2011. I have enjoyed working with you and thank you for many nice lunches and coffee breaks with you! I deeply appreciate receiving so much of positive encouragement and help from Tiina-Liisa Toivanen, Otto Hedström, Mira Markovaara-Koivisto and Jalle Tammenmaa.

I am extremely grateful to my family and friends, especially my parents and my sister, who have always believed in me. Finally, I would like to thank my husband Antti for listening me and keeping things in perspective.

Espoo, 30 November 2016  
Eeva Huuskonen-Snicker





# Contents

Acknowledgements.....	5
List of Abbreviations.....	9
List of Symbols .....	11
Author's Contribution.....	14
1. Introduction.....	15
1.1 Background to non-destructive evaluation of pavement compaction with the GPR.....	15
1.2 Objectives and scope.....	18
2. Theoretical background.....	21
2.1 Overview of electromagnetism and microwaves .....	21
2.2 Dielectric permittivity.....	22
2.3 Conductivity .....	24
2.4 Magnetic permeability .....	24
2.5 Wave properties of EM field .....	26
2.6 Effective permittivity and EM mixing models.....	27
2.7 Measurement principles of permittivity .....	29
2.7.1 Resonator measurement principle.....	30
2.7.2 Transmission configuration .....	30
2.7.3 Reflection configuration.....	31
2.8 Depth resolution .....	36
3. Materials and methods.....	39
3.1 Overview .....	39
3.2 Obtaining relative permittivity of thin layers from the surface reflection .....	40
3.2.1 Microwave radar rover .....	40
3.2.2 Microwave radar testing and air voids of drilled asphalt samples .....	42
3.3 Independent measurements of magnetic and dielectric properties of rock specimens utilizing radio frequencies .....	46
3.3.1 Rock specimen origin and preparation .....	46

3.3.2	Cavity resonator set-up for measuring permittivity .....	47
3.3.3	Test arrangements for measuring magnetic permeability ..	49
3.4	Effective permittivity measurements of granular specimens at microwave frequencies .....	51
3.4.1	Preparing of specimens for VNA testing.....	51
3.4.2	Determination of bulk densities and the volume of air for the plastic granule specimens .....	54
3.4.3	Measuring the effective permittivity with VNA scanner configuration .....	54
3.4.4	Verification of VNA scanner configuration with the TDR principle and stripline jigs .....	56
3.5	Asphalt samples selected for the VNA scanning and air void measurements .....	57
4.	Results .....	61
4.1	Microwave radar testing .....	61
4.1.1	Microwave radar measurements .....	61
4.1.2	Comparison measurements for microwave radar testing in Yläne .....	62
4.2	Permittivity and permeability of studied rock specimens.....	65
4.2.1	Dielectric permittivity results .....	65
4.2.2	Magnetic permeability results .....	65
4.3	Effective permittivity results of granular specimens .....	67
4.3.1	Effective permittivity results of plastics .....	67
4.3.2	Effective permittivity of asphalt aggregate and filler specimens .....	70
4.3.3	Effective permittivity of selected asphalt samples.....	72
5.	Discussion .....	73
5.1	Reliability and validity of current GPR method in QC of thin overlays .....	73
5.2	Implications of increasing the depth resolution capabilities ..	75
5.3	Implications of permittivity and permeability variations in rocks .....	76
5.4	Implications of grain size .....	77
5.5	Issues related to polarization of electromagnetic wave.....	78
6.	Conclusions .....	81
	References .....	83

# List of Abbreviations

AC	Dense graded asphalt mixture
AlMg3	5754 aluminium alloy
CMP	Common midpoint method
CRIM	Complex refractive index model
DIM	Dimensions
EM	Electromagnetic
EPS	Expanded polystyrene
Fe <sub>3</sub> O <sub>4</sub>	Magnetite
GPR	Ground-penetrating radar
HMA	Hot mix asphalt
KDE	Kernel density estimation
K <sub>u</sub> band	12-18 GHz frequency range
LC	Inductor (L), capacitor (C) (circuit)
NDT	Non-destructive testing
PANK	Finnish Pavement Technology Advisory Council ( <i>Päällystealan neuvottelukunta ry in Finnish</i> )
PTFE	Polytetrafluoroethylene, Teflon
POM	Polyoxymethylene
QA	Quality assurance
QC	Quality control
R	Receiving antenna
SI	International System of Units
SMA	Stone mastic asphalt, also coaxial connector type
SSD	Saturated surface dry

T	Transmitting antenna
TDR	Time domain reflectometry
UV	Ultraviolet
VNA	Vector network analyzer

# List of Symbols

$A$	Reflection amplitude
$A_m$	Reflection amplitude from metal
$B$	Magnetic flux density (T), Bandwidth (Hz)
$C$	Capacitance
$c$	Speed of light in vacuum, $3.00 \cdot 10^8$ m/s
$D$	Electric flux density (C/m <sup>2</sup> ), Diameter (m)
$d$	Thickness (m)
$E$	Electric field strength (V/m)
$E_{inc}$	Incident electric field strength
$E_{refl}$	Reflected electric field strength
$f$	Frequency (Hz)
$f_c$	Centre frequency (Hz)
$f_r$	Resonant frequency (Hz)
$f_{ro}$	Resonant frequency of the empty resonator (Hz)
$H$	Magnetic field strength (A/m)
$J$	Current density (A/ m <sup>2</sup> )
$k$	Calibration factor
$L$	Inductance
$P$	Power
$R_{loss}$	Resistance causing losses ( $\Omega$ )
$Q_d$	Dielectric quality factor
$Q_l$	Loaded quality factor

$Q/Q_o$	Quality factor change
$V$	Volume (m <sup>3</sup> )
$V_a$	Air void content (%)
$W$	Pulse width (s)
$v$	Velocity (m/s)
$\alpha$	Attenuation (1/m)
$\Gamma$	Reflection coefficient
$\Gamma_{\perp}$	Reflection coefficient for perpendicular polarization
$\Gamma_{\parallel}$	Reflection coefficient for parallel polarization
$\Delta r$	Depth or range resolution (m)
$\varepsilon$	Dielectric permittivity, permittivity (F/m)
$\varepsilon_e$	Permittivity of the environment
$\varepsilon_i$	Permittivity of the inclusion
$\varepsilon_r$	Relative permittivity
$\varepsilon'_r$	Real part of relative permittivity
$\varepsilon''_r$	Imaginary part of relative permittivity
$\varepsilon'_{r,eff}$	Effective relative permittivity
$\varepsilon_o$	Permittivity of free space, $8.85 \dots \cdot 10^{-12}$ F/m
$\varepsilon^*$	Complex permittivity
$\eta$	Intrinsic impedance
$\theta_i$	Incident angle
$\theta_t$	Transmission angle
$\lambda$	Wavelength (m)
$\mu$	Magnetic permeability
$\mu_r$	Relative permeability
$\mu'_r$	Real part of relative permeability
$\mu''_r$	Imaginary part of relative permeability
$\mu_o$	Permeability of free space, $4\pi \cdot 10^{-7}$ H/m
$\mu^*$	Complex permeability
$\rho$	Charge density (C/m <sup>3</sup> )

$\rho_b$	Bulk density (kg/m <sup>3</sup> )
$\rho_m$	Solid or maximum density (kg/m <sup>3</sup> )
$\sigma$	Electrical conductivity, conductivity (S/m)
$\tau_g$	Group delay
$\phi$	Phase shift (rad)
$\chi_m$	Magnetic volume susceptibility
$\omega$	Angular frequency (rad/s)



## Author's Contribution

The author was responsible for analysing the laboratory and road measurement results presented in this work. The discussion and conclusions in this work are based on the analysis of the author. The sample preparation for magnetic permeability measurements, road measurements with the microwave radar and preparing the granular plastic specimens were done by the author. The geological background information and petrophysical properties of rocks were studied by the author. This study was partly made in a research project "Pavement Life Cycle Research Program, Assessment of Asphalt Pavement Density". Therefore, the planning of the road and laboratory measurements as well as the VNA measurements and derivation of those permittivity results were done in co-operation during the research project.

# 1. Introduction

## 1.1 Background to non-destructive evaluation of pavement compaction with the GPR

Ground-penetrating radar (GPR) is an electromagnetic probing and imaging method of subsurface. History and various GPR applications have been summarized for example in (Daniels 2004; Annan 2003). The GPR have generally been applied in geology (Benson 1995), sedimentology (van Overmeeren 1998; Neal 2004; Gibbard et al. 2009), hydrogeology (Nakashima et al. 2001; Huisman et al. 2003), glaciology (Moore et al. 1999), and peatland research (Hänninen 1992; Jol & Smith 1995; Holden et al. 2002). Furthermore, the common GPR applications are related to the detection of landmines which has been studied by i.e. (Bruschini et al. 1998; Gader et al. 2001; Yarovoy et al. 2007; Takahashi et al. 2011; Podd et al. 2015). In civil engineering, the GPR method has been applied to study roads, including structural layers and pavements, bridges, railways, concrete structures and tunnels (Saarenketo 2009; Pajewski et al. 2013; Bungey 2004; Zhang et al. 2010; Siren et al. 2015). GPR applications can basically be divided into locating objects inside structures and to non-destructive testing (NDT) and evaluation of materials. For example, detecting voids or reinforcements in concrete with GPR have been reported (Barrile & Pucinotti 2005; Shaw et al. 2005; He et al. 2009; Maierhofer 2003; Cassidy et al. 2011). Material testing includes applications such as the moisture content evaluation of concrete (Laurens et al. 2002; Laurens et al. 2005; Klysz & Balayssac 2007; Hugenschmidt & Loser 2008) and the compaction degree evaluation of asphalt pavements (Saarenketo & Scullion 2000).

The most commonly employed GPR type is the pulse radar, which is based on transmitting electromagnetic pulses with a centre frequency ranging from 50 MHz to over 2 GHz depending on the application. In road surveys, 1 GHz technology with horn antennas is typically applied (Saarenketo 2006). Frequency range of the system is important as it impacts the penetration depth of the signal and the resolution capabilities. Higher frequency results in better resolution, but the penetration depth is then reduced. The amplitude and arrival time of the reflected pulse is measured, and saved for further analysis.

Being a non-destructive method is a major benefit of GPRs. This means that destructive coring can be avoided or decreased by adopting the radar method. Furthermore, instead of studying limited amount of core specimens from restricted locations, with the radar the studied structure can be measured extensively. Yet another benefit of the radar is related to the work safety, particularly

in road environment. The GPR system can be mounted in a van and operated along the traffic. This reduces the need of hazardous work on the road.

When GPR is used for evaluating material properties, the dielectric permittivity of the material is calculated from the measurable electromagnetic signal properties, such as amplitude. The permittivity is then processed into the desired quantity, such as air voids or moisture content, through experimental calibration equations or electromagnetic volumetric mixing models. Variety of calibration equations and mixing models exists (Sihvola 1999; Tsui & Matthews 1997; Leng 2011). An example of experimental model is the Finnish PANK calibration method for evaluating air voids of newly laid asphalt pavements (PANK-4122), which is accepted by the Finnish pavement technology advisory council (PANK).

In Finland, the GPR is nowadays a commonly used quality control (QC) method for studying the air void content of newly laid asphalt pavements. The air void content is the volumetric proportion of air in the asphalt. As the pavement is compacted, the volume of air is decreasing. The importance of the compaction and, therefore, the air void content is related to the long-term performance and durability of the pavement (Huang 1993; Doré & Zubeck 2009). The GPR method is based on deriving the relative permittivity, also known as dielectric constant, from the radar surface reflection, and then calculating the air void content from the permittivity based on calibration core results (Fig. 1). The Finnish specification (PANK-4122) was originally released in 1999, and updated in 2008. The English translation of the specification can be found in (Sebesta et al. 2013). The very first field tests were reported by Saarenketo (1997) and further field and laboratory studies leading to accepting this guideline was conducted by Roimela (1998) in 1996-1997. Results of these studies indicated an exponential correlation between asphalt air voids and the measured dielectric constant of the pavement. Fig. 1 summarizes the PANK procedure of determining air void content from the GPR measurements.

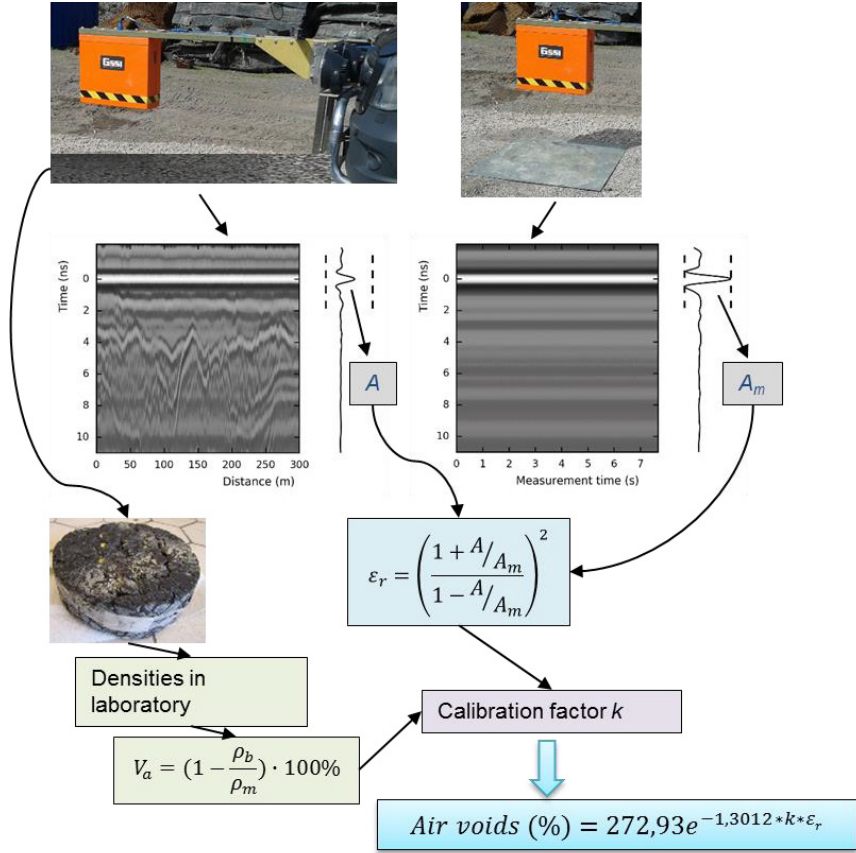


**Figure 1.** Diagram of Finnish PANK calibration method for calculating air voids ( $V_a$ ) of asphalt pavement from GPR surface amplitude ( $A$ ) data. The calibration factor ( $k$ ) is determined based on the air voids and relative permittivity ( $\epsilon_r$ ) of the drilled asphalt sample.

Recently, more studies have been published about the compaction degree, that is the air void content in other words, evaluation with GPR. Leng et al. (2011) have tested different electromagnetic mixing models for calculating the bulk specific gravity from the GPR data with 2 GHz antennas, which does not enable good enough depth resolution for thin pavement layers. The detailed model derivation and validation has been explained in (Al-Qadi et al. 2010). Fauchard et al. (2015) have also been employing volumetric mixing models to evaluate the compaction degree of the pavement. In their research, broader frequency range and step frequency radar, instead of the commonly applied 1 or 2 GHz systems, were implemented. This implementation was, however, achieved with laboratory scale equipment utilizing a vector network analyser (VNA). Permittivity properties of asphalt pavements have also been studied at remarkably higher frequencies related to the research of automotive radars (Sarabandi et al. 1997; Brunett et al. 2003). Automotive radar sensors at frequency bands of 24 and 77 GHz have been developed for driver assistance systems such as adaptive cruise control and collision warning (Meinel 1995; Hasch et al. 2012).

Non-destructive testing of pavements with GPR also requires understanding of typical road materials and structures. Asphalt pavements are actually composite materials made of rock aggregates, fine mineral fillers, and bitumen. The air void content depends on the asphalt type. The average air voids of stone mastic asphalt (SMA) for example should be between 2 and 5 % (PANK 2011). Voids in asphalt or in other road layers can be partially or completely filled with water depending on the weather conditions and the road structures (Doré & Zubeck 2009). Furthermore, different side products like fly ash and slag, or recycled asphalt masses can be used as well.

Another characteristic is the layered road structure, which can be constructed of several layers of unbound and bound bearing layers, pavement layers, and the thin asphalt wearing course on the top of the road structure (see for example Huang 1993). An example of the road structure is illustrated in Fig. 2. Different layers vary in thickness from tens of centimetres to the only 40-50 mm thick wearing course. Furthermore, different layers are far from homogenous as they consist of rock materials with varying grain sizes and mineralogical compositions. The largest nominal grain size of aggregates is typically 16 mm, or even 22 mm for pavements. These distinct material properties should be acknowledged when GPR method is applied. Instead of assuming homogenous media, we should be talking about heterogeneous, granular and layered media.

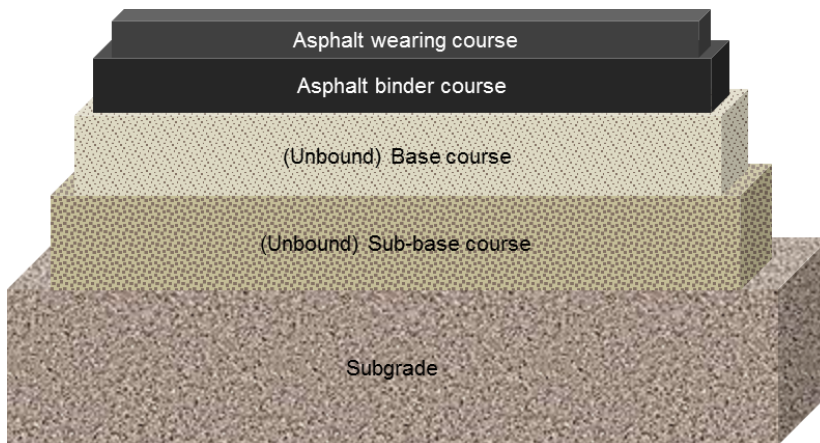


**Figure 2.** An example of the road structure with different unbound and bound layers. The thickness of layers range from centimetres to tens of centimetres.

## 1.2 Objectives and scope

The objective of this study is to analyse if ground-penetrating radar, or microwave technology in general, can be applied in air void content assessment of thin granular asphalt pavement layers, based on the measured effective permittivity. Furthermore, this study aims to provide an understanding about factors affecting effective permittivity measurements of heterogeneous, granular and layered media. The scope of this study is to consider radar applications from the perspective of road structures in Finland. More detailed research questions are formulated as follows:

- Is the currently applied GPR method reliable and valid in QC of thin overlays?
- Could higher frequencies, even above 10 GHz, be exploited in QC of thin overlays?
- Which implications follow from the permittivity and permeability variations in rocks in terms of QC of thin overlays?
- What are the consequences of the large grain size of rock aggregates compared with the applied frequencies?

Outcome of this study can also be used to assess if effective permittivity is a useful parameter in NDT of other rock aggregate based materials such as concrete. Commonly, it is assumed that the variation in permittivity results is directly related to material variation under interest, such as changes in air void content. This may not be a valid assumption when permittivity results are used for non-destructive testing and evaluation. In Fig. 3, different subareas contributing to the permittivity readings are comprised.

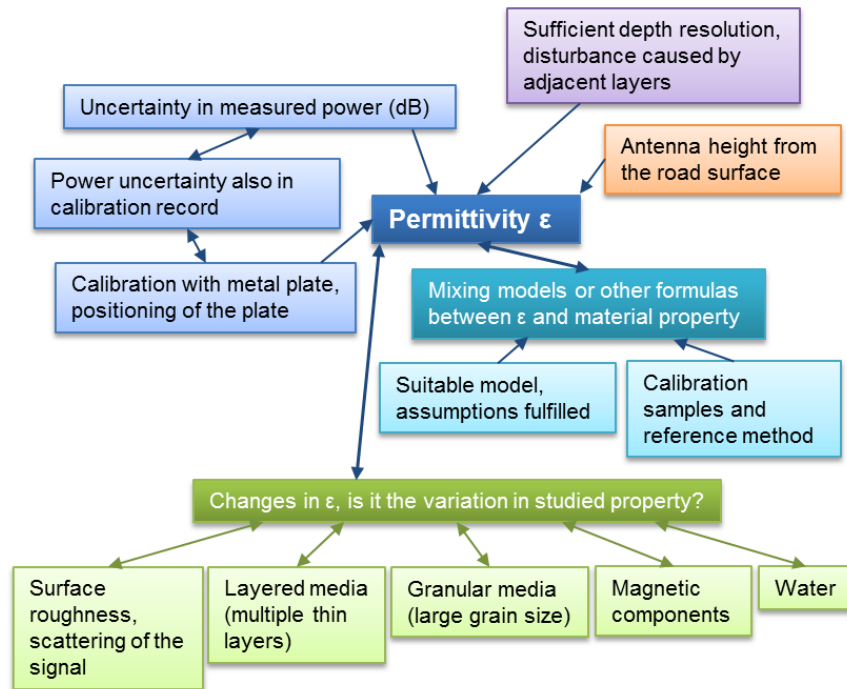


**Figure 3.** Factors causing uncertainty and variation in permittivity measurements.

The studied materials and methods are explained in the beginning of Section 3.1, in addition to the reasoning behind the chosen research approach. In this study, an experimental approach was applied as it was strongly encouraged by the project partners. Other possibility would have been numerical modelling, which might have saved experimental work, but is time consuming as well. A profound concern relates to the insufficient depth resolution of the traditional

GPR systems which is presented in Section 2.8. This is particularly problematic when thin dielectric layers are studied. Therefore, a higher frequency radar with centimetre scale depth resolution was developed and is presented in Section 3.2.1. To validate the permittivity readings at the higher, 7-17 GHz frequency band, laboratory tests were conducted. In Sections 3.3 and 4.2, the potential impact of the magnetic permeability in permittivity results is studied for selected rock type. In Sections 3.4 and 4.3, the effect of material granularity is discussed. This becomes an issue when depth resolution is improved and heterogeneous thin layers are studied.

Permittivity is not directly measurable quantity with radar or other electromagnetic measurement principles. The measured quantity is typically power or amplitude, and possibly signal phase. The uncertainty related to the measurement of power is explained in Section 2.7.3. Chapter 5. provides a comprehensive analysis of different factors shown in Fig. 3 affecting permittivity results.

## 2. Theoretical background

### 2.1 Overview of electromagnetism and microwaves

Electromagnetic (EM) radiation covers a broad frequency range decreasing from the highest X-rays, ultraviolet (UV) radiation, visible light, infrared radiation to the lowest radio waves. Microwaves are defined as frequencies from approximately 1 GHz to 100 GHz. Generally applied ground-penetrating radar frequencies from 50 MHz to 2 GHz lie in the lower limit of this range. More commonly microwaves are used in telecommunications.

Theoretical foundation of ground-penetrating radar is essentially related to the basic theories of electromagnetics. GPR method is based on the propagation and attenuation of EM field in the subsurface. Maxwell's equations (1-4) formulate basis for the propagating EM fields: a time-varying magnetic field induces an electric field, similarly like changing electric field gives rise to a magnetic field

$$\nabla \cdot \mathbf{E} = \frac{\rho}{\varepsilon_0}, \quad (1)$$

$$\nabla \cdot \mathbf{B} = 0, \quad (2)$$

$$\nabla \times \mathbf{E} = -\frac{\partial \mathbf{B}}{\partial t}, \quad (3)$$

$$\nabla \times \mathbf{B} = \mu_0 \left( \mathbf{J} + \varepsilon_0 \frac{\partial \mathbf{E}}{\partial t} \right), \quad (4)$$

where  $\mathbf{E}$  is the electric field strength (V/m),  $\mathbf{B}$  the magnetic flux density (T),  $\mathbf{J}$  the current density (A/m<sup>2</sup>),  $\rho$  the charge density (C/m<sup>3</sup>),  $\varepsilon_0$  the permittivity of free space, and  $\mu_0$  is the permeability of free space.

In a vacuum where no currents or charges are present, these equations reduce to

$$\nabla \cdot \mathbf{E} = 0, \quad (5)$$

$$\nabla \cdot \mathbf{B} = 0, \quad (6)$$

$$\nabla \times \mathbf{E} = -\frac{\partial \mathbf{B}}{\partial t}, \quad (7)$$

$$\nabla \times \mathbf{B} = \mu_0 \varepsilon_0 \frac{\partial \mathbf{E}}{\partial t}. \quad (8)$$

If we take the curl of Eq. (7), and use the curl of the curl,

$\nabla \times (\nabla \times \mathbf{A}) = \nabla(\nabla \cdot \mathbf{A}) - \nabla^2 \mathbf{A}$ , we get



$$\nabla \times (\nabla \times \mathbf{E}) = \nabla(\nabla \cdot \mathbf{E}) - \nabla^2 \mathbf{E} = -\frac{\partial \nabla \times \mathbf{B}}{\partial t}. \quad (9)$$

Then, by applying Eq. (5) on the left side,

$$\nabla(\nabla \cdot \mathbf{E}) - \nabla^2 \mathbf{E} = -\nabla^2 \mathbf{E}, \quad (10)$$

and Eq. (8) on the right side of the Eq. (9),

$$-\frac{\partial \nabla \times \mathbf{B}}{\partial t} = -\mu_0 \varepsilon_0 \frac{\partial^2 \mathbf{E}}{\partial^2 t}. \quad (11)$$

We get the wave equation

$$\frac{1}{c^2} \frac{\partial^2 \mathbf{E}}{\partial^2 t} - \nabla^2 \mathbf{E} = 0. \quad (12)$$

In Eq. (12), the speed of light in vacuum is used  $c = 1/\sqrt{\varepsilon_0 \mu_0}$ . As seen from Eq. (12), this coupled interaction of electric and magnetic fields produces propagating waves. In this case, the derivation was done for the electric field vector, but similar derivation can be done for the magnetic part. In a more complex medium, corresponding analysis for the propagating waves can be carried out.

The propagation and attenuation of the electromagnetic radiation, such as transmitted GPR pulse, is determined by electromagnetic quantities of the medium. These quantities are dielectric permittivity  $\varepsilon$ , magnetic permeability  $\mu$  and electrical conductivity  $\sigma$ . A fundamental work by von Hippel (1954) provides the comprehensive theory of the EM fields and dielectric materials. In linear and isotropic media, constitutive equations (Eqs. 13-15) describe the response of the material to the EM field

$$\mathbf{J} = \sigma \mathbf{E}, \quad (13)$$

$$\mathbf{D} = \varepsilon \mathbf{E}, \quad (14)$$

$$\mathbf{H} = \frac{1}{\mu} \mathbf{B}, \quad (15)$$

where  $\sigma$ ,  $\varepsilon$  and  $\mu$  are scalar quantities.  $\mathbf{D}$  is the electric flux density (C/m<sup>2</sup>) and  $\mathbf{H}$  the magnetic field strength (A/m). In general,  $\sigma$ ,  $\varepsilon$  and  $\mu$  are not constant, but they can be dependent on the frequency. In anisotropic media, conductivity, permittivity and permeability are tensors. They can also be dependent on the strength of the applied field in the non-linear medium. Permittivity, conductivity and permeability are further discussed in following Sections 2.2-2.4.

## 2.2 Dielectric permittivity

Dielectric permittivity, or simply permittivity,  $\varepsilon$  (Eq. 14) is a quantity representing response of a material to an electric field. Permittivity is conventionally related to capacitors where electrical energy is stored in dielectric material between the capacitor's conducting plates. In dielectric materials, charged particles are bound and they respond to an electric field by restricted displacement.

This is called polarisation. According to a classical model, the negatively charged electron cloud around the positive nucleus is distorted when an electric field is applied. As the response to an electric field is not instantaneous for real materials, instead of a vacuum, permittivity of material is frequency dependent quantity. Typically, the relative permittivity decreases when the frequency increases at microwave frequencies. The permittivity is, therefore, a complex variable

$$\varepsilon^* = \varepsilon_0 \varepsilon_r = \varepsilon_0 (\varepsilon_r' - j \varepsilon_r'') , \quad (16)$$

where  $\varepsilon_r$  is the relative permittivity of material. The permittivity of free space  $\varepsilon_0$  is approximately  $8.85 \cdot 10^{-12}$  F/m. The real part of relative permittivity,  $\varepsilon_r'$  describes the stored energy and imaginary part,  $\varepsilon_r''$  represents energy losses. Relative permittivity, or just the real part of relative permittivity is also referred as dielectric constant, especially in older GPR literature. As relative permittivity is dimensionless in SI units, it is more commonly used than the permittivity having the unit F/m. In this thesis, the term permittivity is used for the real part only unless otherwise expressed.

Relative permittivity of dielectric materials varies from 1 for air, to 81 for water. To be precise, the relative permittivity of vacuum is exactly 1, but the  $\varepsilon_r$  of air is very close to that. The permittivity properties of free water are related to its polar molecule structure having negative charges on one side and positive charges on another. Free water is, therefore, highly polarizable as polar molecules align and redistribute under the electric field easily. The  $\varepsilon_r'$  and  $\varepsilon_r''$  of water are frequency dependent and follow the known Debye model which is described in (Cassidy 2009), for instance. Basically, the  $\varepsilon_r'$  and  $\varepsilon_r''$  of water are close to constants clearly below 1 GHz frequency, i.e. typical GPR frequency range. In addition, relative permittivity of water is strongly dependent on the temperature, the  $\varepsilon_r'$  of ice being approximately 3.

When relative permittivity of different minerals or soil and rock types is considered, extensive lists can be found from literature (see for example Parkhomenko 1967; Keller 1988; Daniels 2004; Cassidy 2009). Often, listed values are only given for a certain frequency, such as 100 MHz or lower, and the imaginary part is less commonly available. The relative permittivity of rocks is dependent on the mineralogical composition, but the porosity and water content are affecting as well (Schön 1996). The effect of free and bound water in soils and unbound road materials on relative permittivity has been studied by Saarenketo (1998). A wide range exists in relative permittivity values of even one rock type. For example, the relative permittivity of dry granite varies from 5 to 8 (Cassidy 2009), which is a wide range in terms of material evaluation. The permittivity values found in literature can, therefore, be considered average or typical relative permittivities for different materials. Nevertheless, many detailed studies have been reported on the relative permittivity properties of particular rocks (Ulaby et al. 1990; Fauchard et al. 2013) or construction materials (Shang et al. 1999; Soutsos et al. 2001; Jamil et al. 2013), over specific frequency ranges. Fauchard et al. (2013) measured with cylindrical resonant cavities dif-

ferent rock types used in asphalt production in Normandy, France. They measured both the  $\varepsilon'_r$  and  $\varepsilon''_r$  as part of their larger study on compaction estimation with radar. The  $\varepsilon'_r$  of studied rock samples ranged from 4 to 8.

## 2.3 Conductivity

Another quantity of medium describing the response to the electric field, in addition to permittivity, is the electrical conductivity  $\sigma$  (Eq. 13). The conductivity is related to free charges in material creating a conducting current under the influence of an electric field. These are simply free electrons in metals or dissolved anions and cations in fluids. The unit of conductivity is S/m, and it is the inverse of resistivity ( $\Omega\text{m}$ ). In GPR applications, the conductivity is mostly affecting the attenuation of the GPR signal. It is connected to the imaginary part of the relative permittivity

$$\varepsilon''_r = \frac{\sigma}{\omega \varepsilon_0}, \quad (17)$$

where  $\omega$  is the angular frequency. Conductivity can also be a complex quantity having the imaginary part at higher frequencies (Lambot et al. 2004; Cassidy 2009).

Although many minerals, and therefore rocks and soils, are poorly conducting in dry conditions, there is practically always water with dissolved charges in geological materials to some extent. Highly conductive clays are a classical example of the medium which attenuates GPR signals virtually completely. In concrete, water and chloride contents have an influence on the conductivity and attenuation of the GPR signal, which could be used to evaluate the corrosion of concrete reinforcements (Sbartai et al. 2007; Kalogeropoulos et al. 2011). In road pavement evaluation, the effect of conductivity is often neglected. This can be in general assumed as the pavement should be measured with radar in dry conditions. However in practical applications, it can be difficult to estimate the real water content of the pavement since asphalt surface can be rough and porous and water can be absorbed into the pavement.

## 2.4 Magnetic permeability

Magnetic permeability describes the response of a material to the magnetic field (Eq. 15). Materials can be divided into dia-, para-, and ferromagnetic based on their magnetic response. Magnetism is intrinsically related to the spin of atoms. Relative magnetic permeability  $\mu_r$  is the ratio of permeability and permeability of free space  $\mu_0$

$$\mu_r = \frac{\mu}{\mu_0} = 1 + \chi_m, \quad (18)$$

and relative permeability is also related to the magnetic volume susceptibility  $\chi_m$ . Permeability of free space  $\mu_0$  equals to  $4\pi \cdot 10^{-7}$  H/m. Likewise dielectric permittivity and conductivity, the magnetic permeability  $\mu^*$  can be a complex, frequency dependent quantity

$$\mu^* = \mu_0(\mu'_r - j\mu''_r), \quad (19)$$

where  $\mu'_r$  is the real part of permeability and  $\mu''_r$  imaginary part of permeability related to the magnetic losses (Olhoeft & Strangway 1974; Cassidy 2008). Usually when considering GPR applications, relative magnetic permeability is assumed to be close to 1, since most minerals are dia- or paramagnetic. However, the  $\mu_r$  is higher than 1 for some geological materials with high magnetite content for example (Keller 1988; Klein & Santamarina 2000). Magnetite ( $\text{Fe}_3\text{O}_4$ ) is classified as ferrimagnetic material and is the main magnetic mineral in rocks causing magnetic behaviour. Another possible source of magnetic minerals in construction materials is fly ash (Presuel-Moreno & Sagüés 2009).

Asphalt aggregates used in the main roads in Finland have to fulfil strict quality standards in order to resist the abrasion due to the studded winter tires and have good freeze-thaw durability. These properties are related to the rock type of the aggregates, and furthermore to the mineralogy, texture, origin and metamorphism stage of the rock type. Also, the adhesion between aggregates and the bitumen is dependent on the rock type and the mineralogy. Therefore, the Finnish asphalt specifications (PANK 2011) sets some requirements about the mineral content of asphalt aggregates. The portion of rock forming minerals that are easily weathered or soft minerals such as talc, micas and sulphides, is restricted in aggregates. Considering these regulations together with the Finnish bedrock characteristics (Lehtinen et al. 2005; Räisänen 2004; Räisänen & Torppa 2005), usually the best quality aggregates used in asphalt surface wearing course are from mafic to intermediate rock types. In mafic rocks, magnetite is a common accessory mineral (Nesse 2011).

Magnetic properties of rocks, the susceptibility or magnetic permeability, are widely studied (e.g. Schön 1996; Clark 1997; Puranen 1989), since interpretation of measurements based on the magnetic field needs knowledge of these properties. However, traditionally the susceptibility is measured at lower frequencies, around 1 kHz (Pokorný et al. 2011), compared to the common GPR frequencies. Magnetic properties of rocks can be frequency dependent and, therefore, permeability measurements at higher frequencies have a significance.

Recently, some studies have been made to characterize the effect of magnetic permeability on GPR measurements. Cassidy (2008) studied the GPR signal velocity and attenuation by measuring the complex apparent permittivity of quartz magnetite mixtures. In his approach, the effect of the magnetic permeability cannot be separated from the permittivity effects. Therefore, the concept, apparent permittivity, has been introduced which includes effects of dielectric and magnetic properties. This approach is convenient in some cases such as in

numerical modelling (Cassidy & Millington 2009), and in practical GPR applications (Van Dam et al. 2013). However, this approach is not suitable when the knowledge of magnetic permeability exclusively is necessary.

## 2.5 Wave properties of EM field

The EM fields propagate through the medium as waves if the losses are low. At low frequencies, below the specific transition frequency, the diffusion of the EM field occurs. The transition frequency describes when the material response to the electric field changes from the conduction currents to the displacement currents (Annan 2009). Pure wave propagation takes place above the transition frequency, which is the regime where GPR method can be applied. Then, GPR pulses travel without dispersion in the media.

In practical GPR applications, the important EM wave parameters are velocity  $v$  and attenuation  $\alpha$ . The velocity is

$$v = \frac{1}{\sqrt{\epsilon\mu}} = \frac{c}{\sqrt{\epsilon_r'}}, \quad (20)$$

where  $c$  is the speed of light in vacuum ( $3.00 \cdot 10^8$  m/s). The latter part of the Eq. (20) is valid if  $\mu = \mu_0$ . The attenuation is expressed as

$$\alpha = \sqrt{\frac{\mu}{\epsilon}} \cdot \frac{\sigma}{2}. \quad (21)$$

The wavelength  $\lambda$  of the GPR signal in medium can be calculated from the ratio of the velocity and frequency  $f$

$$\lambda = \frac{v}{f} = \frac{c}{f\sqrt{\epsilon_r'}}. \quad (22)$$

In Table 1, the wavelength is calculated for the different  $\epsilon_r'$  values with the three frequencies of 1, 7 and 17 GHz, representing the range of frequencies used in this study. The  $\epsilon_r'$  of 1 corresponds to air, 3 is close to the bitumen, and 5 and 7 different rock types. The velocity is calculated for given  $\epsilon_r'$  values. In Table 1, the unit of velocity is m/ns which is often convenient in practical GPR applications because travel times of GPR pulses are normally in the range of nanoseconds. Resulting from Eq. (22), the wavelength decreases as the frequency or the permittivity increases. In other words, the wavelength in air is larger compared to the asphalt.

The reflection and transmission of the electromagnetic wave at a material interface is an important wave property considering the GPR applications. This topic is further discussed in Sections 2.7.2 and 2.7.3.

**Table 1.** Velocities and wavelengths at given values of the real part of permittivity and frequency.

$\varepsilon'_r$ (-)	Velocity (m/ns)	Frequency (GHz)	Wavelength (m)
1	0.30	1	0.300
1	0.30	7	0.043
1	0.30	17	0.018
3	0.17	1	0.173
3	0.17	7	0.025
3	0.17	17	0.010
5	0.13	1	0.134
5	0.13	7	0.019
5	0.13	17	0.008
7	0.11	1	0.113
7	0.11	7	0.016
7	0.11	17	0.007

## 2.6 Effective permittivity and EM mixing models

Materials encountered in NDT with GPR are often composites having different individual component materials with distinct permittivity properties. A simple mixture is for example composed of grains of solid homogenous material, and air in between the grains. Concrete is a mix of aggregates, cement and water. Another example is asphalt consisting of rock aggregates, mineral fillers, bitumen and air. All of these individual components have their specific permittivity properties. As was already discussed in Section 2.2, the span of  $\varepsilon'_r$  for rock aggregates is wide, e.g. typically from 4.5 to 6.5 (Dolukhanov 1971), and for bitumen between 2.6 and 2.8 (ITT 1977) or approximately 2.7 at 25 °C (Shell Bitumen 1990), while the  $\varepsilon'_r$  of air is close to unity. The macroscopic permittivity response is a combined effect of each component and, therefore, the measured quantity is actually the effective relative permittivity  $\varepsilon'_{r,eff}$ . However, for solid homogenous material, such as plastic, the measured effective permittivity is close to the relative permittivity.

Electromagnetic mixing models describe the permittivity response of heterogeneous media. Basically, all models consist of volumetric portions of component materials in the mixture and their permittivities. Three models were selected to be introduced here, The Maxwell Garnett formula, the linear model and the complex refractive index model (CRIM). The firstly introduced Maxwell Garnett is considered to be the most fundamental model (Sihvola 1999), the CRIM is quite often applied for geological materials and the linear model was chosen to be introduced because of its simplicity. The Maxwell Garnett mixing formula describes the effective permittivity of homogenous medium with spherical inclusions

$$\varepsilon'_{r,eff} = \varepsilon_e + 3V\varepsilon_e \frac{\varepsilon_i - \varepsilon_e}{\varepsilon_i + 2\varepsilon_e - V(\varepsilon_i - \varepsilon_e)}, \quad (23)$$

where  $\varepsilon_e$  is the permittivity of the environment,  $\varepsilon_i$  permittivity, and  $V$  volume fraction of inclusions (Sihvola 1999). One of the simplest models found from literature is the linear model

$$\varepsilon'_{r,eff} = \sum V_n \varepsilon'_n, \quad (24)$$

where  $V_n$  is the volumetric portion and  $\varepsilon'_n$  is the relative permittivity. Another widely known mixing model is the CRIM,

$$\sqrt{\varepsilon'_{r,eff}} = \sum V_n \sqrt{\varepsilon'_n}, \quad (25)$$

which has been applied for some granular geological materials, for example (Cassidy 2009). A more general study about the relationship between granules and bulk density has been conducted by Nelson (2005) who investigated powdered materials. Tsui & Matthews (1997) have presented a modelling study on different analytical mixing models for dielectric properties of concrete. In (Leng 2011), mixing theories have been applied to predict the compaction level of asphalt pavement from GPR data.

Different electromagnetic mixing models (Eqs. 23-25) and the Finnish PANK calibration model are compared in Fig. 4. The mixing results were calculated based on the very simple two material model, where the background medium had 5 for the real part of relative permittivity, and the amount of air varied from 0 to 100 %. The background medium could be composed of asphalt mastic which is the mixture of bitumen and rock aggregates. The experimental PANK model has been plotted for two different calibration factor  $k$  values: 1 and 0.5. Fig. 4 illustrates that differences among the mixing models are quite small compared to the PANK model with distinct  $k$  values. Naturally, models should be compared around 5 % of air voids, which is the magnitude that is interesting in terms of asphalt quality assurance. Interestingly, the PANK model gives physically impossible results requiring the permittivity to be above that of background medium to reach 0 % air voids.

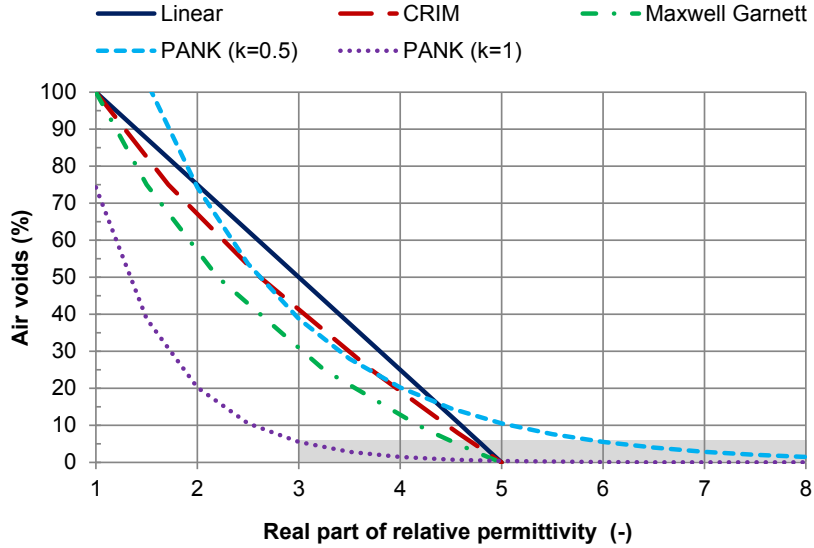


**Figure 4.** Comparison of different electromagnetic mixing models (Linear model, CRIM and Maxwell Garnett) and the Finnish PANK model with two calibration factors ( $k$ ). Mixing models were implemented with  $\epsilon'_s=5$  for the surrounding media and changing the air voids. The most interesting part in the figure is highlighted with grey colour.

An important aspect of applying electromagnetic mixing models is that they are based on specific assumptions that should be fulfilled. For example, the inclusion shape and distance between the inclusions needs to be considered. Furthermore, inclusions in the medium should be small compared to the wavelength (Sihvola 1989). The EM wave, i.e. radar pulse, begins to be affected by individual grains when the wavelength is comparable with the grain size. In this study, it was realized that the largest aggregates in asphalt can be larger or of the order of the radar wavelength at microwave frequencies. With the frequency of 10 GHz and the relative permittivity of 5, the wavelength is approximately 13 mm. This means that if GPR applications normally lie in the Rayleigh scattering regime, we are now dealing with the Mie scattering region and oscillation of amplitude response is possible (Annan 2003). However, electromagnetic mixing models are not intended to consider scattering or multiple reflections.

## 2.7 Measurement principles of permittivity

The relative permittivity of materials can simply be determined by measuring the capacitance of a capacitor having dielectric material between its conducting plates in a case of the static electric field. However, when time-varying electromagnetic fields are addressed, different measurement approaches are needed. At radio and microwave frequencies, measurement techniques can basically be divided into circuit based measurements, transmission line measurements and free space measurements. Resonator measurements belong to the first group. The time domain reflectometry (TDR) measurements are part of the second



group. The last group includes radar and free space measurements in transmission configurations.

In this study, different measurement principles were employed for measuring the effective permittivity of studied materials and specimens. The choice of the suitable measurement principle is affected by the measurement environment, i.e. laboratory or field conditions, obtainable specimen size and available measurement devices. Permittivity measurements based on the resonator principle, are presented in Section 3.3 for studying specific rock specimens. In addition to radar measurements with the new continuous wave radar (Section 3.2.1), free space measurements in transmission configuration were also conducted for various sample types (Section 3.4.3). Verification of the special VNA scanner transmission configuration was conducted with a measurement set-up based on the TDR principle and stripline jigs (Section 3.4.4).

### 2.7.1 Resonator measurement principle

The permittivity measurement with the resonator is based on the resonant frequency shift due to the permittivity properties of the specimen. The resonant frequency is decreased when the specimen is in the resonator compared to the empty resonator. The real and imaginary parts of relative permittivity can be derived from the resonant frequency shift and the quality factor of the resonator. The real part of relative permittivity can be approximated from the resonant frequency  $f_r$  and the resonant frequency of the empty resonator  $f_{r0}$

$$\varepsilon'_r \approx \left( \frac{f_{r0}}{f_r} \right)^2, \quad (26)$$

if the losses are low, thus  $\varepsilon'_r \gg \varepsilon''_r$  (Nyfors 2000). The dielectric quality factor  $Q_d$  is defined as

$$Q_d = \frac{\varepsilon'_r}{\varepsilon''_r}, \quad (27)$$

and describes losses (Nyfors 2000). With the resonator method it is only possible to determine the permittivity for the specific frequency depending on the resonator construction. The resonator method has various industrial applications in evaluation of material properties, including moisture content (Nyfors & Vainikainen 1989; Nyfors 2000; Olkkonen et al. 2012).

### 2.7.2 Transmission configuration

Relative permittivity of the studied specimen can be obtained with the free space measurement in transmission configuration. The EM signal is then transmitted through the studied material, which means that antennas are placed at opposite sides of the specimen (Fig. 5). This limits the application of the method to laboratory conditions in most cases. In comparison, antenna or antennas are at the same side of the studied material in the reflection configuration. Antennas are connected to the VNA, which can be used to accurately measure amplitude

and relative phase angle of the test signal as a function of frequency (Hiebel 2014).

The real part of relative permittivity  $\varepsilon'_r$  is calculated based on the group delay  $\tau_g$  through the specimen when the sample thickness  $d$  is known

$$\tau_g = \frac{d}{v} = \sqrt{\varepsilon'_r} \cdot \frac{d}{c} \quad (28)$$

$$\varepsilon'_r = \left( \frac{c_0 \tau_g}{d} \right)^2. \quad (29)$$

The group delay  $\tau_g$  is obtained from VNA measurements as a function of total phase shift  $\phi$  and angular frequency  $\omega$

$$\tau_g = -\frac{\partial}{\partial \omega} (\phi(\omega)). \quad (30)$$

The more detailed calculus is explained in (Pellinen et al. 2015a).

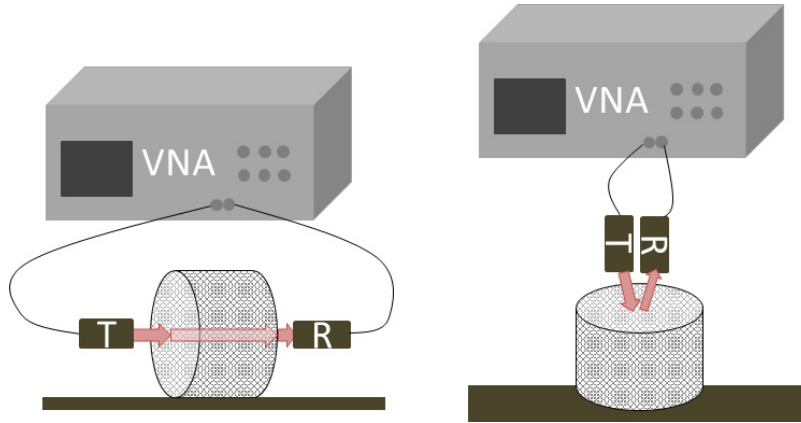


**Figure 5.** *On the left*, a schematic figure of the transmission measurement, where transmitting antenna (T) is on the other side of the sample as the receiving antenna (R). *On the right*, a schematic figure of the reflection measurement, where transmitting antenna (T) is on the same side of the sample as the receiving antenna (R).

### 2.7.3 Reflection configuration

When relative permittivity is obtained based on the reflection measurements, antennas are placed at the same side of the studied material (Fig. 5). Similarly than in transmission measurements, VNA can be utilized as part of the measurement set-up. Furthermore, reflection principle is employed in radar measurements. The transmitted radar pulse is reflected and refracted according to Snell's law on the interfaces where permittivity or permeability properties change. Typical reflecting interface is the asphalt surface when radar antennas are placed in air above the pavement.

With air-coupled antennas, it is possible to extract the relative permittivity from the surface reflection amplitude with respect to the calibration signal assuming a lossless situation (Maser & Scullion 1992). Permittivity of the surface

layer is calculated by comparing the surface reflection amplitude  $A$  to the reflection from a reference conducting metal plate  $A_m$

$$\varepsilon_r = \left( \frac{1+A/A_m}{1-A/A_m} \right)^2. \quad (31)$$

The Eq. (31) is derived from the normal incidence of the plane wave at a conducting and a dielectric plane boundary. Both mediums are considered semi-infinite. The reflection coefficient  $\Gamma$  is defined as the ratio of the reflected  $E_{refl}$  and the incident  $E_{inc}$  electric field strengths and, furthermore, as the ratio of the intrinsic impedances  $\eta_{1,2}$  at a boundary

$$\Gamma = \frac{E_{refl}}{E_{inc}} = \frac{\eta_2 - \eta_1}{\eta_2 + \eta_1}. \quad (32)$$

The intrinsic impedance is determined by  $\mu$  and  $\varepsilon$  of the medium when a perfect dielectric is considered and  $\sigma$  can be neglected

$$\eta = \sqrt{\frac{\mu}{\varepsilon}}. \quad (33)$$

As the amplitude of the incident electric field is unknown in GPR measurements, two equations are needed to solve it and the reflection coefficient. It is assumed that in two different reflections, that are considered, the incident amplitude is the same and reflection occurs from the conducting metal plate (Eq. 34) and dielectric surface (Eq. 35)

$$A_{inc} \cdot \Gamma_{metal} = A_{refl,metal} \quad (34)$$

$$A_{inc} \cdot \Gamma = A_{refl}. \quad (35)$$

The intrinsic impedance of a good conductor equals to 0 (Eq. 33) and, therefore,  $\Gamma_{metal} = -1$  (latter part of Eq. 32). By substituting this to Eq. (34), we get  $A_{inc} = -A_{refl,metal}$ . When this is used in Eq. (35), the relation for the reflection coefficient is obtained

$$\Gamma = \frac{A_{refl}}{-A_{refl,metal}}. \quad (36)$$

The following subscripts are rephrased for simplicity:  $A_{refl} = A$  and  $A_{refl,metal} = A_m$ . By combining Eqs. (32) and (36) for the reflection coefficient, Eq. (37) is obtained

$$\Gamma = \frac{A}{-A_m} = \frac{\eta_2 - \eta_1}{\eta_2 + \eta_1}. \quad (37)$$

If magnetic properties of the medium can assumed to be  $\mu_{1,2} = 1$ , Eq. (37) simplifies to

$$\frac{A}{-A_m} = \frac{1/\sqrt{\varepsilon_2} - 1/\sqrt{\varepsilon_1}}{1/\sqrt{\varepsilon_2} + 1/\sqrt{\varepsilon_1}} = \frac{\sqrt{\varepsilon_1} - \sqrt{\varepsilon_2}}{\sqrt{\varepsilon_1} + \sqrt{\varepsilon_2}}. \quad (38)$$

When the medium 1, before the boundary, is air,  $\varepsilon_1 \approx 1$  and, we obtain

$$\frac{A}{-A_m} = \frac{1 - \sqrt{\varepsilon_2}}{1 + \sqrt{\varepsilon_2}}. \quad (39)$$

By rearranging the Eq. (39), the Eq. (40) is obtained

$$\varepsilon_2 = \left( \frac{-A_m - A}{A - A_m} \right)^2 = \left( \frac{1 + A/A_m}{1 - A/A_m} \right)^2. \quad (40)$$

As can be seen from the previous derivation of the Eq. (31), several assumptions were made to simplify the geometry of the measurement set-up and the material properties of the medium. The smooth plane boundary condition is satisfied according to (Lahouar 2003) at 1.5 GHz using Rayleigh criterion. However, fulfilment of this criterion might become an issue with increasing frequencies and rough asphalt surfaces. The scattering from rough surfaces in GPR pavement applications has also been studied by (Pinel et al 2015; Sun et al 2015).

If we take into account that in most GPR measurement set-ups the transmitting and receiving antennas are separate, the assumption of normal incidence should be replaced with an oblique incidence. Then, the polarization of the incident field also affects the solution of the reflection coefficient. The derivation of these equations, referred to as Fresnel reflection coefficients, can be found e.g. in (Balanis 1989). The reflection coefficients for the perpendicular

$$\Gamma_{\perp} = \frac{E_{r0}}{E_{i0}} = \frac{\eta_2 \cos \theta_i - \eta_1 \cos \theta_t}{\eta_2 \cos \theta_i + \eta_1 \cos \theta_t}, \quad (41)$$

and parallel polarization

$$\Gamma_{\parallel} = \frac{E_{r0}}{E_{i0}} = \frac{\eta_2 \cos \theta_t - \eta_1 \cos \theta_i}{\eta_2 \cos \theta_t + \eta_1 \cos \theta_i}. \quad (42)$$

include the incident,  $\theta_i$  and transmission,  $\theta_t$  angles with respect of normal incidence.

The Eq. (31) is widely used and, for example, as part of the Finnish PANK calibration method in QC of asphalt air voids (see Fig. 1). In theory, this surface reflection method is accurate when the previously mentioned assumptions are fulfilled, but there are some serious limitations when the method is applied in practice. According to Maser & Scullion (1992), Eq. (31) is valid when layers are homogenous and non-conductive. The latter assumption is usually valid for dry asphalt layers, but homogeneity of asphalt layers is a questionable assumption. However, if the conductivity of the medium is not negligible, the intrinsic impedance of the medium is a complex quantity,

$$\eta = \sqrt{\frac{j\omega\mu}{\sigma + j\omega\varepsilon}}, \quad (43)$$

and Eq. (43) instead of Eq. (33) should be applied. In the case of lossy media, the incident and reflected fields need to be modified to take attenuation into account (Balanis 1989).

Another limitation of Eq. (31), which is rarely discussed, concerns the measurement accuracy of power or amplitude. The error of any function with multiple variables,  $F(x_1, x_2, \dots)$  can be determined with the help of total differential  $dF$  and known errors,  $\Delta x_1, \Delta x_2, \dots$ , when an indirect measurement principle is applied. By taking the absolute values of each component and summing them, the maximum value for the error can be estimated

$$\Delta F(x_1, x_2, \dots) = \left| \frac{\partial F}{\partial x_1} \right| \Delta x_1 + \left| \frac{\partial F}{\partial x_2} \right| \Delta x_2 \dots \quad (44)$$

This analysis is based on the assumption that variables are independent.

By applying Eqs. (44) and (31), an expression for the relative permittivity error estimate is obtained

$$\Delta \varepsilon_r(A, A_m) = \left| \frac{\partial \varepsilon_r}{\partial A} \right| \Delta A + \left| \frac{\partial \varepsilon_r}{\partial A_m} \right| \Delta A_m. \quad (45)$$

After calculating the partial differentials, we get

$$\Delta \varepsilon_r = \left| \frac{4A_m(A+A_m)}{(A_m-A)^3} \right| \Delta A + \left| \frac{4A(A+A_m)}{(A-A_m)^3} \right| \Delta A_m. \quad (46)$$

Since  $A < A_m$ , the latter term of the Eq. (46) becomes smaller than the first term. Furthermore, it can be assumed that  $\Delta A_m \ll \Delta A$  when the metal plate reflection is carefully measured for longer period. Therefore, the first term in Eq. (46) is sufficient to estimate the error of the relative permittivity. The Fig. 6 demonstrates how the error of the calculated relative permittivity  $\Delta \varepsilon_r$  is dependent on the measured amplitude and its error  $\Delta A$ . It was calculated by assuming that  $A_m$  is unity and the normalized  $A$  varies. If  $\Delta \varepsilon_r$  should be less than 0.1 units, for example,  $\Delta A$  should approximately be less than 0.01 for  $\varepsilon_r=2.25$ . For materials with higher relative permittivity,  $\Delta A$  should even be smaller, which could be challenging for single measurements on the road.

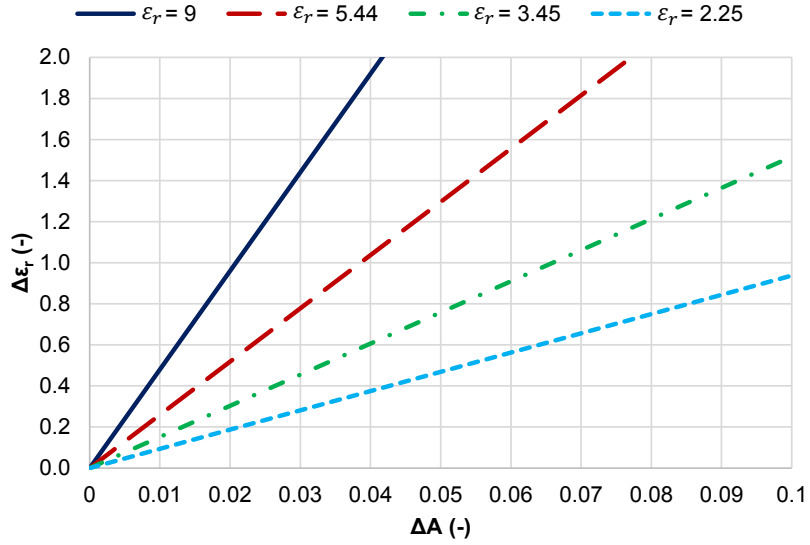


**Figure 6.** The Eq. (46) was used to calculate the effect of  $\Delta A$  on the error of the relative permittivity when  $\Delta A_m \ll \Delta A$ .

The uncertainty in measured power is essentially related to the radar electronics and their drift. At 1-2 GHz frequencies, the error of high-quality instruments in measured power should remain  $\pm 0.5$  dB of the nominal value (Pellinen et al. 2015a). This error limit is, however, considered for the laboratory environment, whereas radar measurements on road conditions have different error levels. In a recent study by Fauchard et al. (2015), the drift of a 2 GHz GPR system was presented that showed the relative permittivity to vary approximately between 4.5 and 4.9 when radar was kept steady. They concluded that the accuracy of a commercial 2 GHz GPR is not adequate to estimate the compaction of asphalt pavements. Poikajärvi et al. (2012) have also reported longer period preheating tests affecting amplitude recordings of GPR devices. In Fig. 7, the effect of power uncertainty is illustrated with three nominal relative permittivity values. The change in power values is used to calculate with Eq. (31) the observed permittivities with respect to real permittivity values. If the real asphalt relative permittivity is 5, the observed value could be from 4.5 to 5.5, with the  $\Delta P = \pm 0.5$  dB. It is also worth noting that when the nominal permittivity increases, also the error or the range in observed permittivity grows.

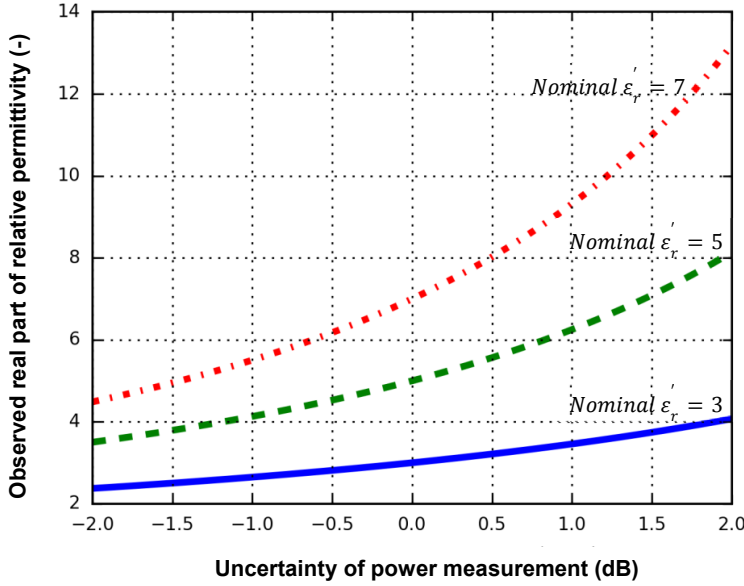


**Figure 7.** The effect of measurement error in power to the observed permittivity with three nominal relative permittivities. The plotted values are calculated with Eq. (31).

## 2.8 Depth resolution

Resolution capabilities of radar systems are defined differently in horizontal and vertical, i.e. depth directions. In terms of material evaluation of thin layers, the depth resolution of the radar system becomes an important parameter. When the permittivity of the material is determined from reflection amplitudes, as discussed in the previous Section 2.7.3, the reflection from the material interface should not be interfered with other, deeper reflections. Otherwise, the layers below the upper most one will have an effect on the permittivity results that can either increase or decrease the reflection amplitude and, thus, the relative permittivity. The depth, or range, resolution  $\Delta r$  of the pulse GPR is defined as proportional to the pulse width at half amplitude  $W$  and velocity  $v$  in material (Annan 2009)

$$\Delta r \geq \frac{Wv}{4} = \frac{v}{4B} = \frac{v}{4f_c}. \quad (47)$$

The pulse width, unit being second or often nanosecond, is inversely proportional to the bandwidth,  $B$  and centre frequency,  $f_c$ ,  $W=1/B=1/f_c$ . By substituting the common centre frequency in pavement applications, 1 GHz, and the material velocity of 0.15 m/ns, corresponding asphalt relative permittivity in Eq. (47), the depth resolution is 0.037 m. It seems to be about the thickness of thin asphalt layers. However, Eq. (47) follows from the idea that if received pulses are separated by half of the pulse width, they are likely interpreted as separate reflections. Pulses are still overlapping and interfering in this case, which may increase or decrease the surface reflection amplitude. Therefore, this approach

is more suitable for identifying subsequent reflections than to be used in material evaluation.

According to Koppenjan (2009), the depth resolution is defined as

$$\Delta r = \frac{1.39c}{2B\sqrt{\epsilon_r}}, \quad (48)$$

which is a semi-empirical equation. Eq. (48) provides the lower boundary of the depth resolution for any practical applications. The calculated depth resolution is now 0.104 m, for the velocity of 0.15 m/ns and centre frequency of 1 GHz (Eq. 48). This value clearly exceeds the thinnest asphalt layer thicknesses. In conclusion, it can be estimated that the actual depth resolution is between the answers provided by Eqs. (47-48).

Yet, many references have indicated that the surface reflection with 1 GHz GPR is only affected by the uppermost 0-30 mm (Sebesta et al. 2013, p. 19), or approximately at most 50 mm (Hoegh et al. 2015). Another approach to address the depth resolution question was presented by Pellinen et al. (2015a), where depth resolution was simulated with transmission line models. The half power pulse width of 1 ns was noticed to be inadequate for correctly determining the relative permittivity of the 4 cm thick asphalt layer.

If the depth resolution of the radar is inadequate compared to the layer thickness, a radar with increased depth resolution is needed in QC of thin layers compared with the traditional pulse GPRs. The obvious solution is to either shorten the transmitted pulse or to increase the frequency bandwidth, which in turn decreases the pulse width. In practice, it is easier to also increase the centre frequency when increasing the bandwidth. This increased centre frequency, however, affects the wavelength to become shorter (Eq. 22), and the antenna footprint is decreased. As discussed in Section 2.6, the shortened wavelength may produce problems when heterogeneous and granular materials are studied, which is the case with asphalt pavements. The antenna footprint is the illumination area of antennas and by reducing it the spatial coverage is reduced. This may cause problems in quality control as well. In conclusion, the adequate depth resolution is essential when evaluating the radar method in QC of asphalt layers.





## 3. Materials and methods

### 3.1 Overview

The depth resolution of commercial 1-2 GHz GPR systems seems to be inadequate for the quality control of thin asphalt pavement layers, as discussed in Section 2.8. Therefore, a new radar was developed and is presented in Section 3.2.1. The first test measurements on roads, however, revealed that there is a large variation in relative permittivity values of pavements. From a theoretical point of view (Section 2.6), the observed change in relative permittivity should be small if air void content of the pavement is around 5 %. This resulted in various laboratory tests which were designed to clarify the relative permittivity variations of granular heterogeneous materials.

When the air void content of asphalt pavement is evaluated based on the measured effective permittivity, the maximum of  $\varepsilon'_{r,eff}$  should not exceed the relative permittivity of the individual components. If this is the case, something is not properly taken into account, or something is disturbing permittivity measurements. In a previous study by Pellinen et al. (2015b), it was observed that the effective permittivities of hot mix asphalt (HMA) samples were exceeding the relative permittivity of rock aggregate it was made of (Olkkonen et al. 2015). Three possible explanations exist for this phenomenon. Firstly, there might be water pockets inside the porous asphalt samples, as the permittivity of water is 80. In this case, this was not probable since samples were kept in dry conditions for a long period before the permittivity measurements. However, it is possible that small water pockets are formed inside the pavement during the construction, and water can only evaporate from voids that are connected.

Secondly, the magnetic permeability of aggregates might have had an impact on permittivity measurements. Therefore, the aim was to measure the magnetic permeability and dielectric permittivity of rock specimens independently from each other. These applied measurement set-ups utilize frequency range comparable to the GPR frequencies. Regarding the QC of asphalt pavements, the possible magnetic effect of aggregates has not been discussed previously. In Section 3.3.2, a cavity resonator is presented for measuring the complex permittivity of rock specimens. The LC resonator test arrangements are designed for permeability measurements of rock specimens and presented in Section 3.3.3.

The third explanation would be the influence of large aggregate granules causing multiple reflections, and thus apparently increasing the effective permittivities. A series of laboratory tests were performed with the vector network ana-

lyzer to measure the effective relative permittivity of air-particle mixtures at microwave frequencies from 7 to 17 GHz. The novelty is to use homogeneous plastic materials and granulate them to imitate the granular composition of non-homogeneous rock aggregates. In addition to plastics, mixtures of air and rock aggregates, as well as mineral filler and air were measured. This laboratory study is presented in Section 3.4.

Fig. 8 summarizes different measurement principles and studied materials employed in this study. Studied materials include asphalt raw materials that are rock specimens, filler and aggregate specimens, drilled asphalt samples from test roads and old as well as new asphalt pavements. Resonator based surveys included both magnetic permeability and relative permittivity measurements, for rock specimens. Most of the laboratory based studies were free space measurements with the VNA transmission configuration. These studies were verified with a set-up based on the TDR principle and stripline jigs. Outdoor measurements consisted of the microwave radar tests.

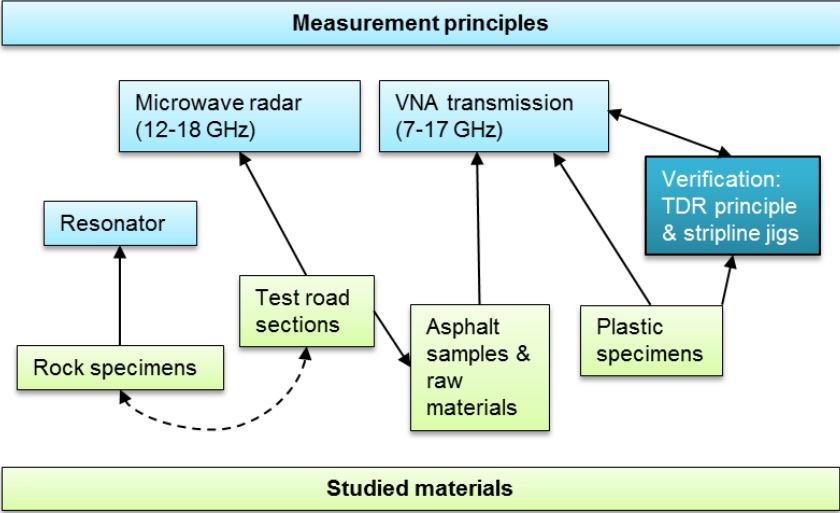


**Figure 8.** Diagram shows how different measurement principles and studied materials are connected in this study.

### 3.2 Obtaining relative permittivity of thin layers from the surface reflection

#### 3.2.1 Microwave radar rover

A novel sweeping microwave radar rover was presented in (Huuskonen-Snicker et al. 2015). The aim of this radar assembly was to produce a low cost radar with good depth resolution for the quality control of thin asphalt layers. The novelty was to use microwave frequencies from 12 to 18 GHz, for obtaining the real part of permittivity from the surface reflection of the pavement. The selected frequency band, the  $K_u$  band, was the first experimental choice because of the affordable radar design and available modules.

The microwave radar was first introduced in 2014, when it was installed on a pulled cart (Olkkonen et al. 2014). The first road testing campaign during the summer 2014 revealed (Fig. 9), however, that positioning of individual measurements was difficult. Therefore, the radar was mounted on a radio controlled car (Fig. 10) for the summer 2015. The assembly ensured also that the physical radar antenna stability was improved, as the car was relatively heavy and rigid. The car length was 800 mm, and the width 500 mm. The car weighed 13 kg with batteries.



**Figure 9.** The 12-18 GHz microwave radar installed on a pulled cart on a test site in 2014.



**Figure 10.** The 12-18 GHz asphalt radar rover on test sites during the summer 2015. Radar antennas point towards the road in front of the remote controlled car.

The radar is quasi-monostatic having separate, but identical transmitter and receiver antennas. They are installed in front of the car, 140 mm above the studied surface. The sweep band is from 12 to 18 GHz with 256 frequency steps. From every measurement point, reflected signal amplitude and the trigonometric cosine of its phase angle are recorded, and through the telemetry link saved for the further analysis. The data processing steps are described in detail in (Hartikainen et al. 2016a)

A calibration signal is needed to calculate relative permittivities from the saved radar data (Eq. 31). Detailed explanation of the reflectivity calibration principles is given by Scheer (1983), and Knott et al. (1993) discusses phenomena related to real reflecting material surfaces. The original idea was to use metal plate for calibration. This was quickly observed to be less successful as the calibration with polyoxymethylene (POM) plastic. The reflection amplitude

from the POM material is closer to that of pavement. In comparison, the reflected amplitude from metal is much higher (Fig. 11). Therefore, the dynamic range requirement for the radar electronics is less demanding when using plastic. Other advantages follow from discarding the metal plate calibration, one of them being the positioning of the calibration plate. The calibration plate needs to be aligned perpendicularly to the antennas and this might be a challenge in outdoor conditions. Furthermore, multiple reflections from the metal plate surface are more difficult to eliminate than the weaker reflections from the plastic. Fig. 11 illustrates the comparison of the metal and POM reflection amplitudes, with respect to a measurement without a sample. The POM calibration block had the surface area of 250 mm x 250 mm, and the thickness of 63 mm.

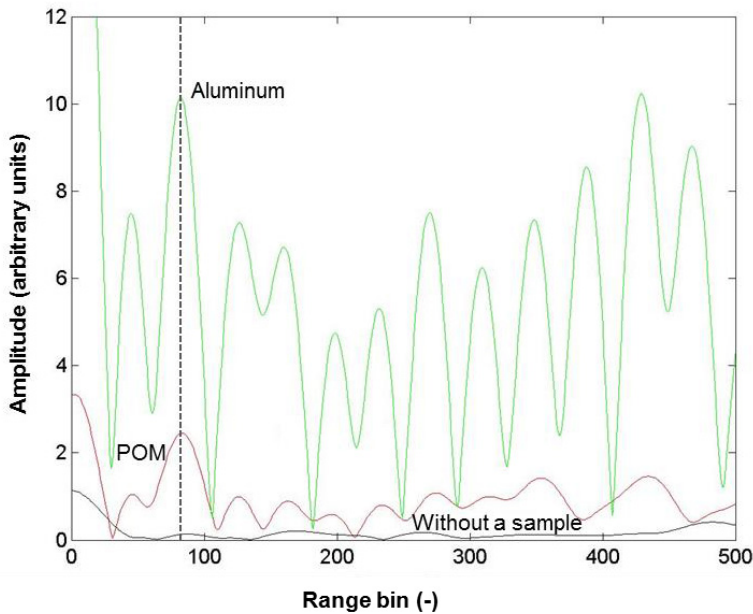


**Figure 11.** Comparison of calibration signals from aluminium (green) and plastic (POM) (red) plates. The reflection distance is marked with a dashed grey line. The black line shows measurement without a sample. Dynamic range of the radar must be expanded if a conducting sheet is chosen for the reflection reference instead of some known dielectric material.

### 3.2.2 Microwave radar testing and air voids of drilled asphalt samples

The novel microwave radar presented in the previous section was tested on various road sections around Finland during summers 2014-2015. In this thesis, measurements from one location only are presented as an example showing permittivity variations along the road surface. Other microwave radar tests are reported by Pellinen et al. (2016) and Hartikainen et al. (2016b). Air void and effective permittivity results of selected drilled asphalt samples from different test sites are nevertheless compared in this work (Section 4.3.3).

The presented test site was located in Yläne, in southwest Finland, in road 210. Microwave radar testing in Yläne was part of the GPR comparison tests organized by the Finnish Transport Agency in 2014. The aim of comparison tests was to measure the same road sections with GPR systems of different contractors, and then compare calculated air void contents. With the microwave radar it was not possible to measure the whole road section and, therefore, only at most 200 m over each drill core location was measured from the right wheel path at six locations. The schematic figure of the radar testing locations are shown in Fig. 12. The first part of the line names refers to the measurement direction and the latter part to the road address. Although the line naming is rather complicated, it was kept identical with the naming presented in the report by Pellinen et al. (2016). The measurements were done in two parts on 28.7.2014 and on 5.8.2014, since rain interrupted the first measurement session. Microwave radar results from Yläne site are presented in the Section 4.1.1.

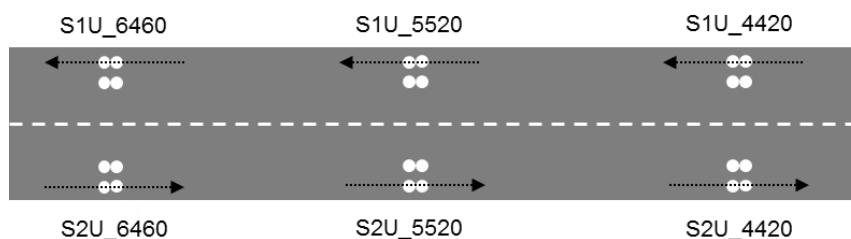


**Figure 12.** Schematic map of microwave radar lines and line naming in Yläne. White circles indicate where asphalt samples were drilled with respect to black microwave radar lines.

White circles in Fig. 12 represent locations where asphalt samples were drilled. From each location, two adjacent samples were taken which are denoted with letters *a* and *b*. Asphalt samples were approximately taken from the right wheel path and between the wheel paths. The letter *U* in the sample name was used for samples from the right wheel path and letter *K* for samples between the wheel paths respectively. Fig. 13 shows a picture from the road after the sampling when the drilling spots were already patched. Altogether 24 samples were drilled with the 100 mm diameter. As microwave radar was only used for measuring the right wheel path, results of those asphalt samples are shown in this work. Air void and density results of other samples can be found from the report by Pellinen et al. (2016).

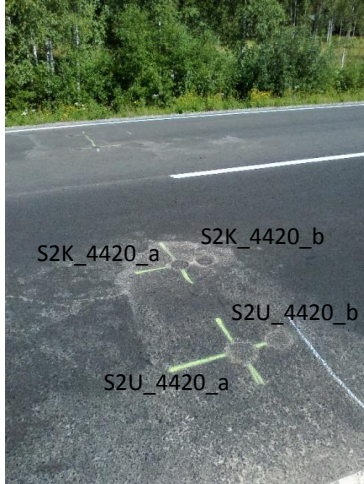


**Figure 13.** Asphalt samples with 100 mm diameter were drilled from Yläne having two adjacent samples a and b. The samples were taken from the right wheel path and between the wheel paths approximately. The text in the picture refers to sample names.

The bulk and maximum densities of drilled asphalt samples were measured in the laboratory. Although the asphalt mixture of Yläne samples was the dense graded (AC) mixture type, the bulk density was obtained with the four different methods: saturated surface dry (SSD), dry, dimensions (DIM) and parafilm according to (SFS-EN 12697-5; SFS-EN 12697-6). Dry method is normally used for the dense graded mixtures. With all methods the asphalt core mass is obtained by weighing the sample in air. The volume of the sample is then obtained by weighing the sample in air and water. The only exception is the dimensions method, in which the volume is calculated from the measured core dimensions. With the SSD method, the air voids are filled with water as the sample is kept in water for some time before the weighing in water. In the dry method, the sample is not immersed in water before the weighing. In the parafilm method, the sample is wrapped with the waterproof plastic before weighing. The bulk density is finally calculated from the sample mass and volume. The maximum density is determined from the asphalt mass which does not take into account the volume of air voids. The air void content  $V_a$  of the specimen can be calculated by comparing the bulk density,  $\rho_b$  to the solid density, or maximum density, of the material,  $\rho_m$

$$V_a = \left(1 - \frac{\rho_b}{\rho_m}\right) \cdot 100\% . \quad (49)$$

Air voids were calculated based on the four different bulk densities for samples from Yläne (Table 2). In Fig. 14, air voids determined with different methods are compared for each sample from the right wheel path. In this case, all the air void results are rather low from 0.5 to 3.5 with the dry method. The average is 1.9 % and the standard deviation 0.6. However, there are differences in calculated air voids depending on which measured bulk density was used in the calculation.

**Table 2.** Bulk densities with four different methods (SSD, dry, dimensions and parafilm), maximum density and respective air voids of drilled asphalt samples from Yläne.

SAMPLE	$\rho_b$ (kg/m <sup>3</sup> )				$\rho_m$ (kg/m <sup>3</sup> )	$V_a$ (%)			
	SSD	DRY	DIM	PARAF.		SSD	DRY	DIM	PARAF.
S1U_6460_a	2454	2452	2424	2412	2482	1.1	1.2	2.3	2.8
S1U_6460_b	2434	2430	2396	2394	2461	1.1	1.2	2.6	2.7
S2U_6460_a	2478	2475	2446	2440	2511	1.3	1.4	2.6	2.8
S2U_6460_b	2467	2464	2431	2412	2495	1.1	1.2	2.6	3.3
S1U_5520_a	2449	2444	2409	2401	2498	2.0	2.2	3.5	3.9
S1U_5520_b	2458	2454	2431	2402	2504	1.9	2.0	2.9	4.1
S2U_5520_a	2464	2456	2420	2409	2503	1.5	1.9	3.3	3.8
S2U_5520_b	2465	2462	2433	2421	2512	1.9	2.0	3.1	3.6
S1U_4420_a	2421	2424	2389	2357	2493	2.9	2.7	4.2	5.4
S1U_4420_b	2426	2423	2380	2363	2501	3.0	3.1	4.8	5.5
S2U_4420_a	2437	2437	2427	2375	2488	2.0	2.0	2.4	4.5
S2U_4420_b	2444	2442	2382	2378	2473	1.2	1.3	3.7	3.8
Average	2450	2447	2414	2397	2493	1.8	1.9	3.2	3.9
Standard deviation	0.017	0.016	0.021	0.024	0.015	0.6	0.6	0.7	0.9

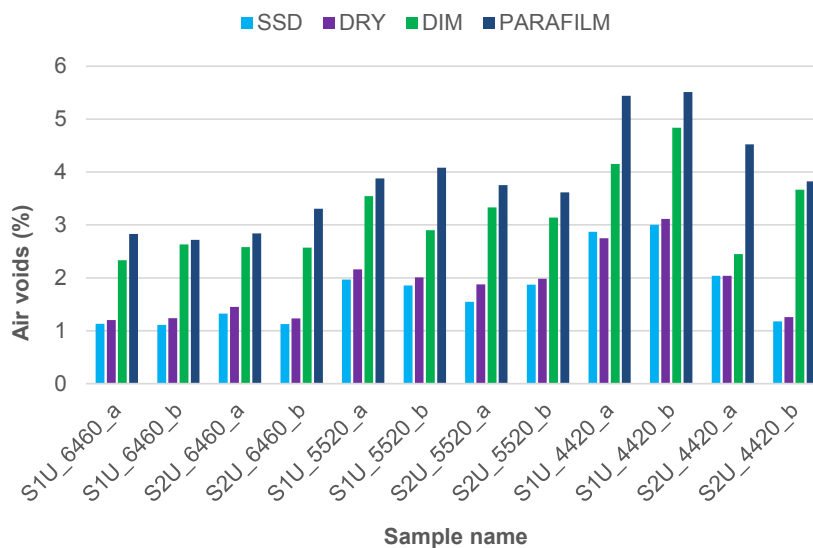


**Figure 14.** Comparing the air void results of samples from Yläne. The bulk density of samples was determined with four different methods.



### 3.3 Independent measurements of magnetic and dielectric properties of rock specimens utilizing radio frequencies

#### 3.3.1 Rock specimen origin and preparation

The studied rocks were collected from a specific quarry located north-west from the city of Tampere, in Finland, as part of the project reported in (Pellinen et al. 2015a). The quarry is used as a source of high quality asphalt aggregates. Rock specimens from the same quarry were also studied in (Olkkonen et al. 2015).

The geological characterization indicated that the studied rock type is metavolcanic rock with intermediate composition. In this rock type, the main minerals are plagioclase and hornblende amphibole. Magnetite occurs as accessory mineral. The rock type characterization was also confirmed by the bedrock map of Finland, scale 1:200 000 (Geological Survey of Finland 2016), which showed that the general rock type around the quarry area is intermediate volcanic rock. Although the quarry area is located in the Central Finland granitoid complex, metavolcanic rocks also exist in that region. These Svecofennian Paleoproterozoic rocks are 1.96–1.75 Ga in age. The original volcanic texture of the rock is still distinguishable, although metamorphism, recrystallization, has affected the texture or the mineralogy. The texture of the metavolcanic rock is composed of a very fine-grained matrix but larger grains of plagioclase and hornblende can be found.

A rock boulder was chosen for drilling the samples for permeability measurements and later for sawing the samples for the permittivity measurement. Originally, the drilling spots were chosen, so that the susceptibility measured with Bartington's MS3 Magnetic Susceptibility Meter with MS2E Core Logging Sensor indicated higher values compared with the general rock mass (Fig. 15a). The operating frequency of this device is 2 kHz. The aim was to find the highest magnetic permeability values that could potentially affect GPR measurements. From the piece of rock, six cylinders were drilled with a nominal diamond drill diameter of 12 mm (Fig. 15b). The cylinders were drilled in three different orthogonal directions, so that the dependency on the measurement direction could be quantified. However, the rock type appeared to be visually rather homogenous and isotropic in composition. Specimens were labelled with names A1-A6.

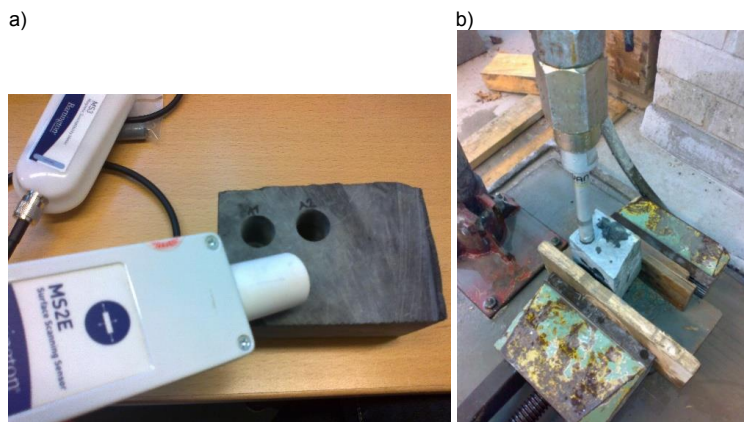


**Figure 15.** a) Magnetic susceptibility measurement with a commercial equipment. b) Rock specimens for permeability measurements were drilled with a 12-mm diamond drill bit.

After the magnetic measurements, small rock specimens described as "buttons" were cut from the cylindrical specimens for placing them in the cavity resonator for permittivity measurements. The buttons were carefully cut from the pre-drilled rock cylinders with a high speed micro milling machine (modified Proxxon MF70 with three axis digital position readout) and a diamond cutting disc. The buttons were labelled with corresponding numbers 1-6. All the rock specimens are presented in Fig. 16.

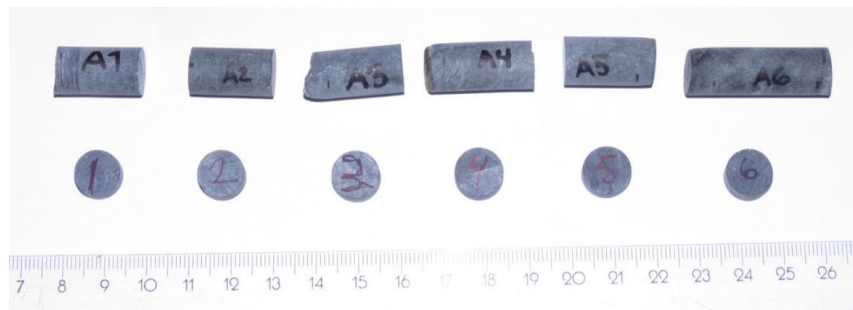


**Figure 16.** The drilled cylindrical rock specimens A1-A6 for the permeability measurement. After permeability measurements, the permittivity was measured from small discs or "buttons" sawn from the cylinders, labelled 1-6. Discs were sawn from the one end of the permeability specimen.

### 3.3.2 Cavity resonator set-up for measuring permittivity

The dielectric properties were evaluated with a cavity resonator shown in Fig. 17. Specimen "buttons" were inserted into the silver coated cavity (diameter 30 mm, depth 25 mm), which has 1 mm coupling loops at opposite points along the circumference. A thin hollow quartz post supports the sample midway between top and bottom covers. Such a cavity works as a parallel resonator at microwaves (Ramo & Whinnery 1956) and a measured response example is illustrated in Fig. 18. In these tests, the signal comes from a HP8350B microwave sweeper

having a HP83597B plug-in and the receiver is HP8757A scalar network analyzer combined with its HP85025A transmission test head (Fig. 19). Frequency reference was obtained from HP5350A counter and power reference from HP435B power meter connected to a HP8481A thermistor sensor.

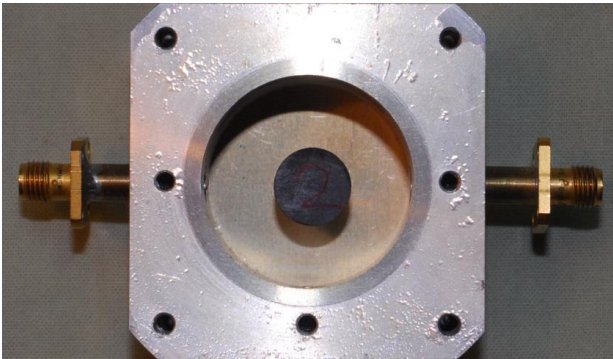


**Figure 17.** Cavity resonator with the rock specimen inserted. Coaxial SMA-type connectors with rigid transmission lines at opposite ends feed two coupling probes.

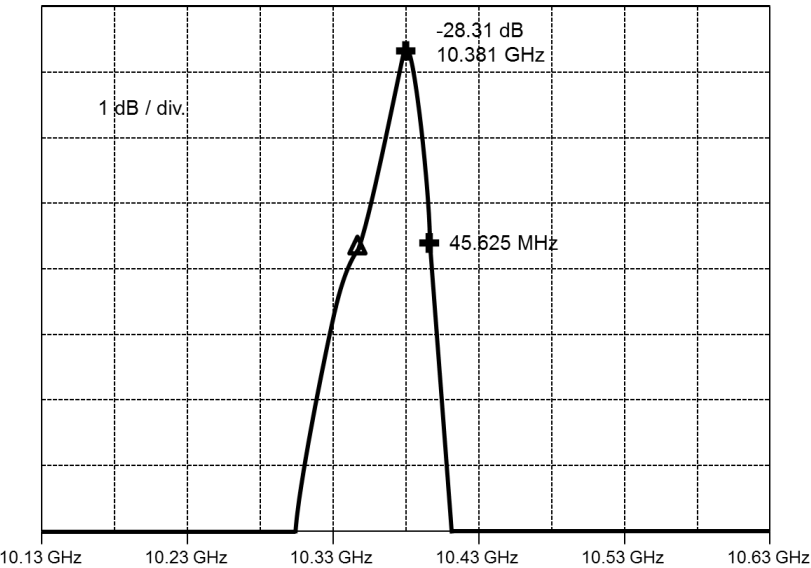


**Figure 18.** An example of measured cavity response. Cursors at resonance peak and 3 dB below it. In this case, the half power bandwidth is 45.625 MHz.

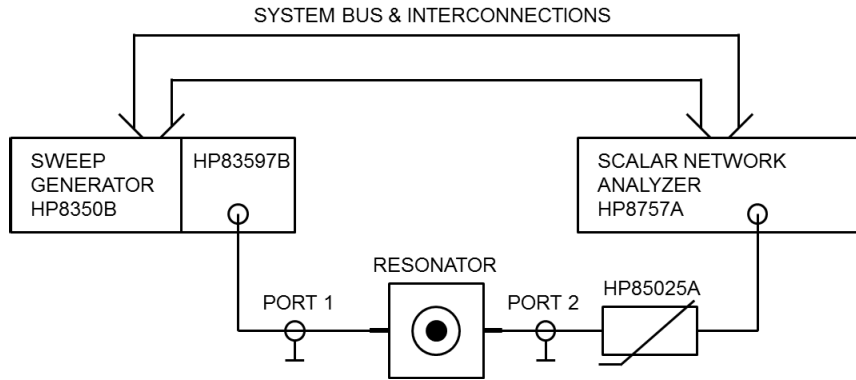


**Figure 19.** Block diagram of the permittivity measurement set-up.

As can be seen from Fig. 18, the scalar analyzer directly indicates resonance frequency and the half power or 3 dB bandwidth of the sample set-up. A variational derivation based on the Itoh-Rudokas model (Itoh & Rudokas 1976; Kajfez & Guillon 1986) was used to get the respective real parts of relative permittivity. Basic resonator theory allows thereafter the computation of approximate loss components, i.e. the imaginary part of the relative permittivity (see for example Nyfors 2000).

### 3.3.3 Test arrangements for measuring magnetic permeability

Three different test arrangements were constructed for the magnetic permeability measurements. A similar approach was used as for the permittivity measurements with cavity resonator set-up. However, the cavity resonator was now replaced with the coil and capacitor in series configuration (Fig. 20). This is called an *LC* resonator, as the coil (*L*) and capacitor (*C*) are separate or “lumped” elements. With this configuration, a strong magnetic field is formed inside the coil and permeability of the sample is calculated from the inductance change compared with the empty coil. Another advantage of the chosen resonator structure is that the magnetic field pattern is predictable when the coil is empty or a sample is placed in it. In Fig. 21, a shunt resonator is shown for 120 MHz, made of insulated copper wire and a high frequency capacitor. The capacitor was placed below the board and is not shown in the photograph. A similar layout but with smaller coils was tried at 250 MHz. A different approach is needed for still higher frequencies as can be seen in Fig. 22. In order to get the stray reactances as small as possible, the coil was placed on the upper side of the board. The one-turn coil is made of wide copper sheet whereby the parasitic inductance can be reduced in comparison with the wire configuration. Detailed resonator data is collected in Table 3. The coil diameter was 12 mm in each case.

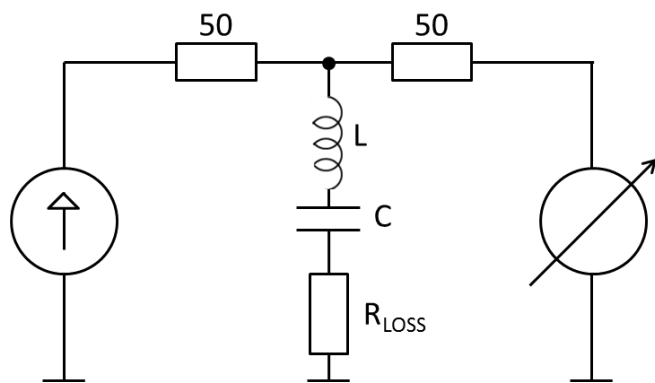


**Figure 20.** Block diagram of permeability measurement set-up.

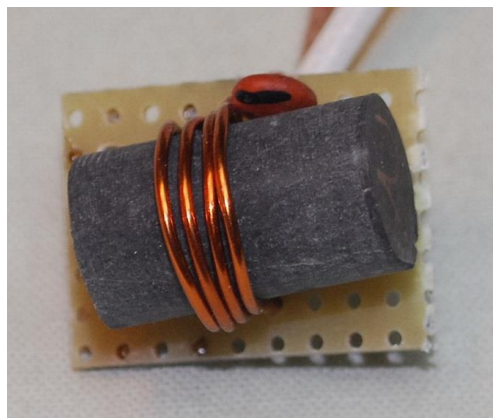


**Figure 21.** LC resonator set-up for 120 MHz measurements. Capacitor is placed below the board.

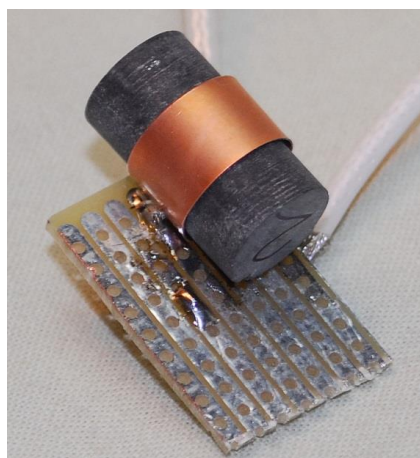


**Figure 22.** LC resonator for 500 MHz tests. In order to get the stray reactances as small as possible, the coil was placed on the upper side of the board.

Table 3. LC resonator parameters.

Parameter	Nominal resonance frequency		
	120 MHz	250 MHz	500 MHz
Coil length (mm)	5	2	N/A
Coil diameter (mm)	12	12	12
Number of turns	3.5	1.5	1
Wire diameter (mm)	0.85	0.85	Strip, w=8, t=0.1
Capacitance (pF)	3.9	3.9	3.9

Similar response measurements were carried out as with the cavities in Section 3.3.2 but in this case HP/Agilent E4421B synthesized signal generator was used as the source because the frequency resolution requirement is more stringent. An example measurement plot is shown in Fig. 23. As the resonators are of the series-shunt configuration, an amplitude minimum is obtained at the frequency of interest. First, the response of the resonator was recorded when the coil was empty and then successively sample cylinders, having a length of 20 mm, were inserted into it. At 500 MHz, the typical down shift was about 5 MHz.

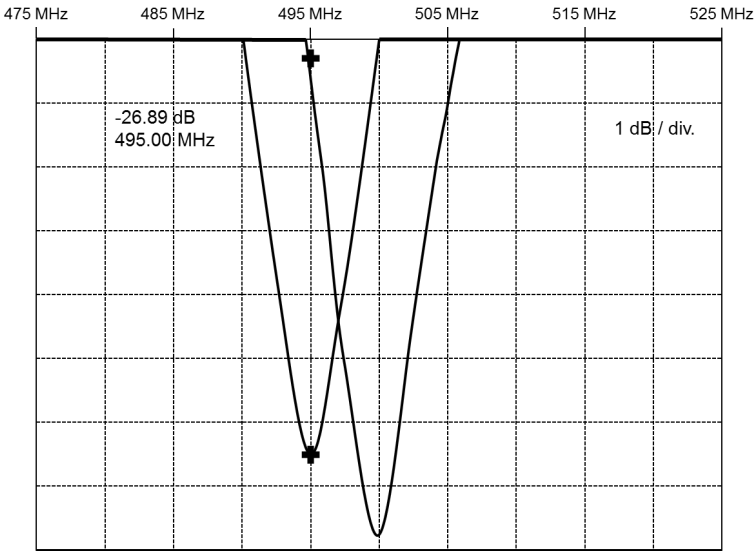


Figure 23. An example of the measured LC resonator response with (left curve) and without (right) rock specimen. With the rock specimen, the resonance drops about 5 MHz and losses increase.

3.4 Effective permittivity measurements of granular specimens at microwave frequencies

3.4.1 Preparing of specimens for VNA testing

The laboratory experiments were designed so that the impact of material granularity compared to the solid form of material, and the influence of empty space

between granules could be tested, particularly regarding our new microwave radar rover. For this part of the study, plastic materials with constant real part of permittivity and known low losses were chosen. The granules of different sizes and materials are shown in Fig. 24a. The plastic used was polyoxymethylene (POM), also known as acetal or polyacetal. Small plastic “cubes” or granules with distinct sizes were sawn from the larger POM plastic plates. The sizes of plastic granules were chosen to imitate the actual rock aggregate fractions used in asphalt production. The nominal plate thicknesses were 5, 10, 20 and 30 mm. Consequently, one of the edge lengths of cubes was close to 5, 10, 20 and 30 mm. The nominal cube sizes were checked afterwards by measuring the three dimensions of some cubes with a digital calliper. Furthermore, 5, 10 and 20 mm cubes were sieved, and Fig. 26 shows the gradation curves.



**Figure 24.** a) From left to the right: polyacetal (POM) sawing waste fibers, 5, 10, 20, and 30 mm POM granules, and rock aggregates. b) 10 mm granules packed in the box without the cover.

Geometry of other granules, besides the 20 mm granules was close to a cube, but the 20 mm granules were actually rectangular cuboids with average dimensions of 21 mm, 9 mm and 16 mm. This type of geometry was chosen because crushed rocks have varying and often elongated shapes. Some of the POM sawing waste was also kept. The sawing waste had a broad size range from fine, dust like particles to over one cm long, thin fibres. The thickness of fibres was less than 0.1 mm.

The POM granules of different sizes were packed in separate, tightly closed cardboard boxes for the measurements. Fig. 24b shows the 10 mm granules in the box without the cardboard lid. All boxes were packed as full as possible, but at same time randomly, trying to avoid the granules to settle in exact rows and piles. Some of the sawing waste was also gathered in boxes and packed at two different bulk densities (later referred as ‘Sawing waste’ A and ‘Sawing waste’ B). Two specimen boxes were prepared so that small granules of expanded polystyrene (EPS) were packed together with POM granules of 5 and 10 mm. In this way, it was possible to increase the air void content of the box and still keep the box tightly packed. It was estimated that EPS does not affect permittivity measurements as its density is low. Cardboard box sizes varied slightly due to the amount of available granules (see Table 4). Other reason was that the amount of the granules packed in a box should be more than just one or two on top of the other.

A blend of rock aggregates and a specimen of mineral filler were obtained as a reference, so that the plastic granule results could be compared with the actual nonhomogeneous rock and mineral materials. Therefore, one box was filled with a blend of actual rock aggregates (Fig. 25a) and another one with limestone mineral filler (Fig. 25b). All aggregate fractions were crushed from the same intermediate metavolcanic rock type. Fig. 26 shows the gradation curve of the blend. The filler fraction (minus 0.063 mm) or portion of mineral filler, typically 5 to 10 % of aggregate blend, was left out from the measured aggregate specimen, and measured as a separate specimen. This was done so that the mineralogical compositions of specimens were as simple as possible.

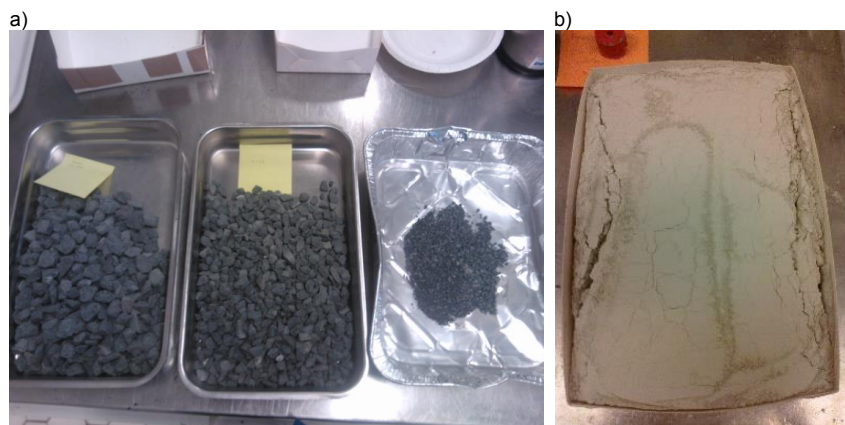


**Figure 25.** a) Fractions of the aggregate blend from left to right 11.2-20 mm, 4-8 mm, and 0.063-2 mm. b) Limestone mineral filler specimen.

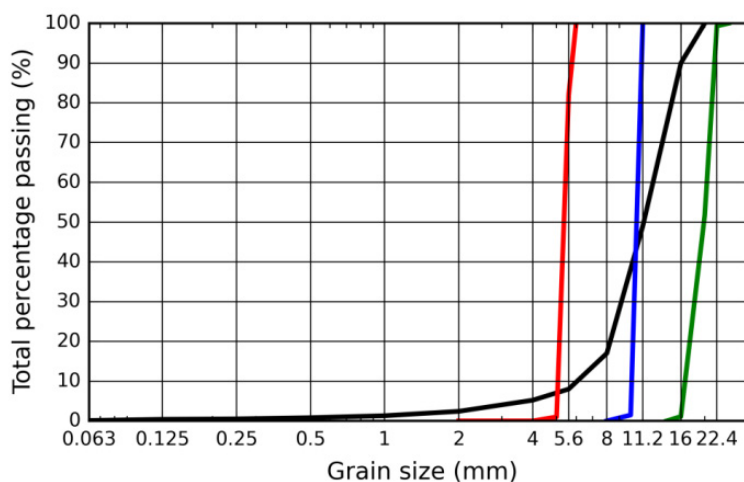


**Figure 26.** Sieving results of the aggregate blend, which has no limestone filler (black), and 5 mm (red), 10 mm (blue), and 20 mm (green) POM granules.



### 3.4.2 Determination of bulk densities and the volume of air for the plastic granule specimens

The volume of the specimen was obtained by measuring the outer dimensions of the box with a digital calliper. In total, six measures were taken in three dimensions, and then the average was calculated. It was estimated that the accuracy of each measure was  $\pm 2$  mm. The bulk density of the specimen was calculated based on the material mass and box volume. The solid density of the POM was determined according to (SFS-EN 1097-7). The air void content  $V_a$  of the specimens was calculated with the Eq. (49).

The air void content of plastic granule specimens is shown in Table 4. The packed sawing waste consisted mostly of air as the  $V_a$  is over 95 %. The air voids in larger granules ranged between 32 % and 65 %. As a specimen box contained only granules of about the same size, the percentage of air voids was rather similar for other specimens than the sawing waste and mixture of POM granules and EPS. By mixing POM and EPS granules, it was possible to increase the air void content of specimens.

**Table 4.** Data used for calculating air void contents of granular POM specimens

	Sawing waste A	Sawing waste B	5 mm + EPS	10 mm + EPS	5 mm	10 mm	20 mm	30 mm
Height (mm)	206 $\pm$ 2	206 $\pm$ 2	206 $\pm$ 2	207 $\pm$ 2	145 $\pm$ 2	205 $\pm$ 2	205 $\pm$ 2	200 $\pm$ 2
Width (mm)	149 $\pm$ 2	146 $\pm$ 2	145 $\pm$ 2	145 $\pm$ 2	117 $\pm$ 2	147 $\pm$ 2	147 $\pm$ 2	199 $\pm$ 2
Thickness (mm)	61 $\pm$ 2	60 $\pm$ 2	60 $\pm$ 2	61 $\pm$ 2	60 $\pm$ 2	62 $\pm$ 2	62 $\pm$ 2	130 $\pm$ 2
Box volume (cm <sup>3</sup> )	1862.0	1798.8	1810.0	1824.7	1009.0	1868.6	1887.6	5180.8
POM density (g/cm <sup>3</sup> )	1.41	1.41	1.41	1.41	1.41	1.41	1.41	1.41
POM mass (g)	96.0	120.3	881.1	1128.3	892.2	1792.5	1752.7	4586.1
Bulk density (g/cm <sup>3</sup> )	0.052	0.067	0.487	0.618	0.884	0.959	0.929	0.885
Air voids (%)	96	95	65	56	37	32	34	37
Air voids, min (%)	96	95	64	54	34	28	31	35
Air voids, max (%)	97	95	67	58	40	35	37	39

### 3.4.3 Measuring the effective permittivity with VNA scanner configuration

The effective permittivity of specimens was measured with a specially designed VNA scanner configuration. The scanner configuration consisted of the vector network analyzer, motorized scanner, two waveguide antennas and laptop. The antennas were placed at both sides of the sample, i.e. results were obtained with the transmission configuration (Fig. 27). The frequency sweep was from 7 to 17 GHz. If the chosen frequency range was lower, the illuminating area of the antenna would be increased and specimens with much larger dimensions would have been needed.

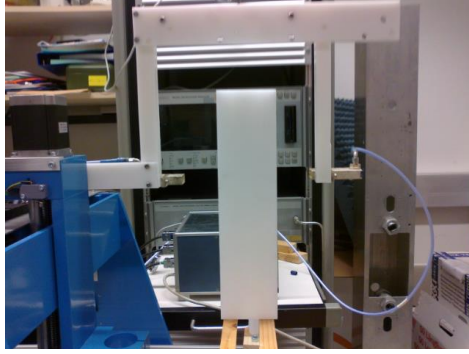


**Figure 27.** The solid POM plate is placed for the VNA transmission measurement in this picture. Antennas are located at the opposite sides of the specimen.

The effective illumination footprint with these waveguide antennas is approximately  $20 \times 20 \text{ mm}^2$  at the selected test distance. However, each of the specimens was scanned so that the antennas were moved with 5 mm steps. Therefore, permittivity results of adjacent measurement points are actually overlapping, because of the larger antenna footprint compared to the measurement point spacing. As a minimum, 100 points were measured from each specimen, from the centre of the specimen. The reflections from the edges may interfere with the incident wave through the specimen and, therefore, the permittivity cannot be calculated reliably near specimen edges. The real part of relative permittivity is calculated with Eqs. (28-30).

Before granular specimens were measured with the VNA scanner configuration, a solid POM plate was scanned as a reference. The plate thickness was 63 mm. The permittivity results are shown as a map in Fig. 28. The average of  $\epsilon'_r$  is 2.84 and the standard deviation 0.01. As seen from Fig. 28, the effective permittivity results have only slight changes between adjacent measurement points and overall, the values are very close to ones found in (Eyraud et al. 2015).

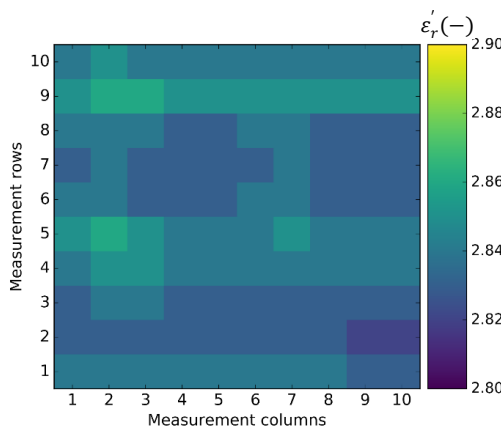


**Figure 28.** Real part of relative permittivity scanning results of the solid POM plate.

### 3.4.4 Verification of VNA scanner configuration with the TDR principle and stripline jigs

Relative permittivity results of the solid POM plate were verified with another measurement set-up based on the time domain reflectometry (TDR) principle with stripline jigs. The idea behind this verification measurement was to develop a set-up that does not require VNA and can be implemented directly in time domain. The measurement configuration consisted of Tektronix 7S12 TDR Sampler, Tektronix S-50 Pulse generator head, Tektronix S-4 Sampling head, Tektronix 7603 Oscilloscope mainframe, Suhner 4901.01.A resistive power divider as well as cables and adapters (Fig. 29). The pulse generator was used to generate a sharp step waveform, the rising edge ideally being half of a Dirac delta signal. In this application, only the sharp front of the signal was enough to ensure the exact calculation of the signal delay through the sample material. Based on the material dimensions and the delay, the relative permittivity of the studied material can be calculated. The construction of a stripline, instead of coaxial cable for instance, was chosen, since it was easier to manufacture a sheet of studied material with exact dimensions compared e.g. with a tube which would have been necessary for a coaxial test sample.

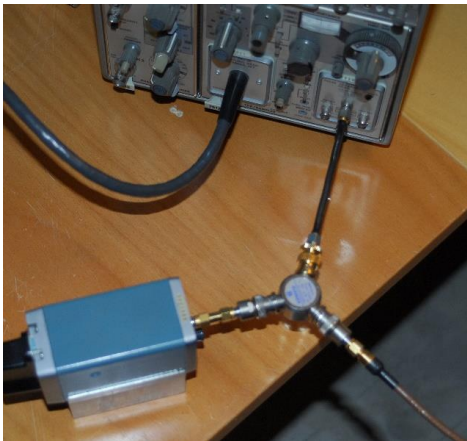


**Figure 29.** The measurement set-up based on the time domain reflectometry (TDR) principle with stripline jigs.

Dimensions of the stripline jig were calculated beforehand based on the expected material permittivity and the available adapter size. The calculation was performed according to Matthaei et al. (1980). The stripline is presented in Fig. 30. It consists of a supporting metal frame of two AlMg3 sheets, and two POM material test sheets in between. Each metal frame was 5 mm thick and 40 mm wide, and a POM sheet 1.9 mm thick and 40 mm wide. A thin copper strip inside the POM plates connected the 3-mm stripline launchers, a male and a female. The copper strip had the thickness of 0.05 mm and the width of 2.1 mm. The total stripline length was 78.3 mm. The closed stripline, which was chosen, diminishes signal losses compared to the mechanically easier microstrip structure. In addition, the stripline was tightly closed so that the air inside the stripline would not disturb the measurement.

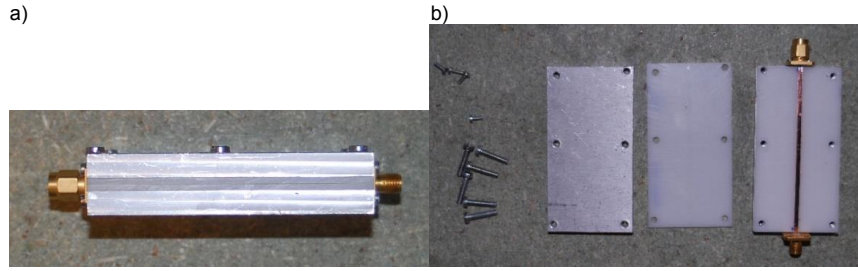


**Figure 30.** a) The closed stripline. b) POM sheets and the connecting copper strip during the assembly process.

The delay within the test set-up was calculated at first. The one-way delay of the coaxial launcher arrangement equals 80 ps, when the PTFE (Teflon) material has the relative permittivity of 2.1 and the total length of 12.0 mm - 2.6 mm + 9.5 mm - 1.9 mm = 17.0 mm, where individual dimensions are taken from manufacturer's technical drawing (Huber+Suhner 2016). Fig. 31 illustrates the measurement result of the studied POM material compared to the reference value. The measured total two-way delay time for POM is  $5.2 * 200 \text{ ps} = 1040 \text{ ps}$ . From this we get  $1040 \text{ ps} / 2 - 80 \text{ ps} = 440 \text{ ps}$  as the stripline one-way value. Now, the calculated relative permittivity equals  $\epsilon_r' = (3 * 10^8 \text{ m/s} * 440 \text{ ps} / 78.3 \text{ mm})^2 = 2.84$ . The calculated value is the same as average of the VNA scanning results.

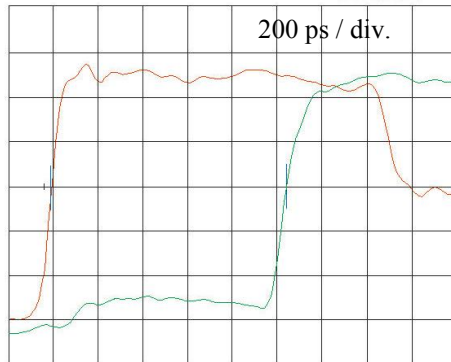


**Figure 31.** The TDR stripline measurement result of POM material is shown with red line and reference measurement with green line. Blue lines indicate the delay of 5.2 divisions equalling 1040 ps.

### 3.5 Asphalt samples selected for the VNA scanning and air void measurements

In the last part of the study, a selection of asphalt samples were scanned with the VNA transmission set-up described in Section 3.4.3. Air voids of these samples were determined in laboratory with bulk density methods described in Section 3.2.2. The scanning was aimed for studying the effective permittivity variations of different asphalt mixtures. Furthermore, the aim was to compare the

scanned effective permittivity results with the traditional air void measurements. Therefore, samples with different origins and mixture types were chosen to be scanned.

Altogether 18 asphalt samples were studied. Densities and air voids of these samples are presented in Table 5. From Yläne test site (Site C), six samples were chosen. They had the AC mixture type as mentioned in Section 3.2.2. Two of the samples (Site A) were actually drilled through all three AC layers and were sawed in separate layers before scanning. From site B, four SMA samples were measured. Two samples were manufactured in laboratory, referred as sites D and E, which are shown in Fig. 32. The samples from sites A-B and D-E had the diameter of 150 mm, and only the Yläne samples (site C) had the 100 mm diameter. The thickness of samples slightly differs, but was typically 40-50 mm. Air voids of all samples varied between 1.1 and 6.9 derived from the SSD bulk density. Comparison of scanned effective permittivity results and air voids are presented in Section 4.3.3.

**Table 5.** Bulk and maximum density as well as air void results of asphalt samples selected for the VNA scanning.

Site	Specimen	$\rho_b$ (kg/m <sup>3</sup> )			$\rho_m$ (kg/m <sup>3</sup> )	$V_a$ (%)		
		SSD	DRY	DIM		SSD	DRY	DIM
A	L-1-A	2275	2287	2219	2418	5.9	5.4	8.2
A	L-1-B	2335	2357	2308	2472	5.5	4.7	6.6
A	L-1-C	2376	2383	2321	2484	4.3	4.1	6.6
A	L-2-A	2253	2276	2202	2421	6.9	6	9
A	L-2-B	2338	2349	2318	2473	5.5	5	6.2
A	L-2-C	2404	2404	-	2484	3.2	3.2	-
B	3.1	2572	2604	2498	2701	4.8	3.6	7.5
B	3.2	2574	2605	2451	2716	5.2	4.1	9.8
B	4.3	2554	2586	2501	2721	6.1	5	8.1
B	4.4	2581	2592	2476	2696	4.3	3.9	8.1
C	S1U_6460_b	2434	243	2396	2461	1.1	1.2	2.6
C	S2U_6460_b	2467	2464	2431	2495	1.1	1.2	2.6
C	S1U_5520_b	2458	2454	2431	2504	1.9	2	2.9
C	S2U_5520_b	2465	2462	2433	2512	1.9	2	3.1
C	S1U_4420_b	2426	2423	2380	2501	3	3.1	4.8
C	S2U_4420_b	2444	2442	2382	2473	1.2	1.3	3.7
D	Specimen D.1	2319	2340	-	2476	6.3	5.5	-
E	Specimen E.1	2430	2429	-	2461	1.3	1.3	-

a)

b)



**Figure 32.** a) An asphalt sample from Site D that is sawn in half for the picture. b) An asphalt sample from Site E. Both samples had the diameter of 150 mm.



## 4. Results

### 4.1 Microwave radar testing

#### 4.1.1 Microwave radar measurements

This section presents microwave test results from Yläne which was one of the selected testing locations (Section 3.2.2). The tests were conducted in two parts, on 28.7.2014 and on 5.8.2014. The studied road had been paved in summer 2014 before radar measurements. Altogether six road sections were measured with the microwave radar, and two out of the six sections on both testing dates. The aim was to measure 200 m in each measurement location along the right wheel path, but because of limited time on the measurement location most of the lines were actually shorter.

Table 6 summarizes information on each measurement line. The new microwave construction was presented in Section 3.2.1. During the first measurement day, the radar was pulled at higher speed so that the average distance between measurement points was 0.19-0.32 m. During the second measurement time, the radar was pulled slower and the average distance between individual sample points was just 0.13 m. The  $\varepsilon'_{r,eff}$  was on average from 3.14 to 4.70, and the standard deviation 0.61-0.98.

**Table 6.** Measurement line information of microwave radar testing on Yläne

Line	Date	Length of the line (m)	Number of measurement points (n)	Average distance between points (m)	Average of $\varepsilon'_{r,eff}$	Standard deviation of $\varepsilon'_{r,eff}$
S1U_6460	28.7.2014	150	588	0.26	3.14	0.61
S2U_6460	28.7.2014	105	553	0.19	4.23	0.86
S1U_5520	28.7.2014	127	411	0.31	3.50	0.92
S2U_5520	28.7.2014	200	626	0.32	3.65	0.98
S1U_6460	5.8.2014	42	336	0.13	3.63	0.64
S2U_6460	5.8.2014	50	398	0.13	4.70	0.82
S1U_4420	5.8.2014	64	507	0.13	4.69	0.77
S2U_4420	5.8.2014	107	865	0.12	4.35	0.87

The microwave radar results are presented as kernel density estimates (KDE) in Fig. 33. The black dashed line indicates the median value of the distribution. The more familiar histogram plot can be understood as a discrete equivalent of the KDE plot. The  $\varepsilon'_{r,eff}$  distribution (Fig. 33) varies for different measurement



locations. On average, the median permittivity values are higher on the second measurement time than on the first time. This might result from the pavement compaction due to the traffic or from moisture increase in the pavement. The latter explanation seems to be more probable since the road had been open for traffic for longer period before both measurements.

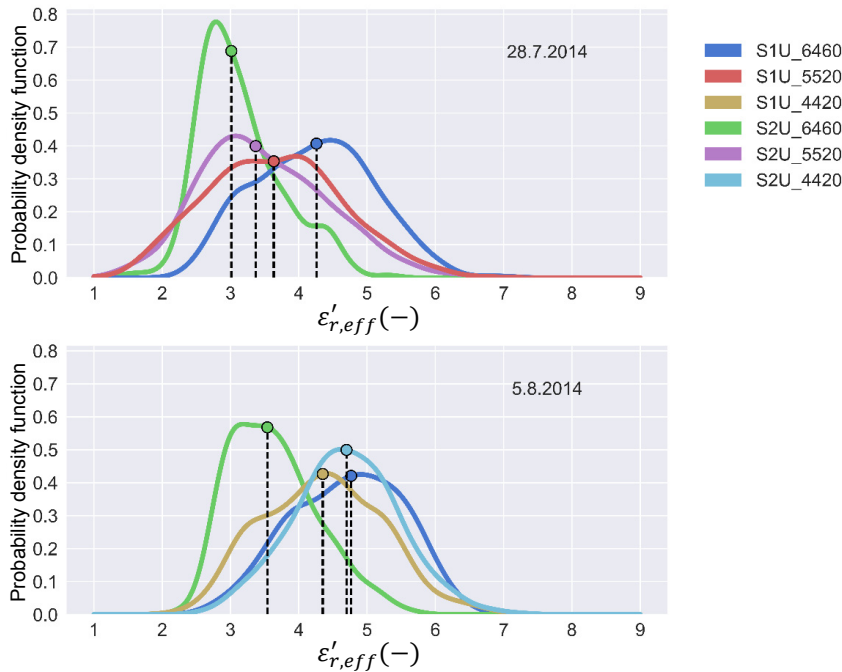


**Figure 33.** Real part of the effective permittivity results from Yläne measured with the microwave radar rover presented as distributions. The black dashed line indicates the median value of the distribution.

The most essential result, however, is the broad range in permittivity values for each measurement line (Table 6 and Fig. 33). GPR results obtained with a commercial equipment from Yläne were reported in (Pellinen et al. 2016), where it was calculated that the average real part of the relative permittivity was 5.59 with standard deviation of 0.25. This is much smaller standard deviation for the entire studied road section than what was measured with the microwave radar for shorter road sections.

#### 4.1.2 Comparison measurements for microwave radar testing in Yläne

The results of the VNA-measurements of asphalt core samples taken in Yläne (see Sections 3.2.2 and 3.4.3 for description of sampling and measurement procedures, respectively) are listed in Table 7 and presented as colour maps in Fig. 34. As drilled samples had the diameter of only 100 mm, the positioning of the sample for the scanning was challenging. Therefore, a small amount of measurement points from the upper right corner of the asphalt core were excluded from the results because the scanning area was too close to the sample edge (Fig. 34). The measurements near the sample rim were disturbed by the edge effects

and are not reliable. The average real part of effective permittivity varies between 5.11 and 6.05 for different samples. The standard deviations range from 0.65 to 0.80.

**Table 7.** Statistics of VNA scanning measurements of Yläne samples.

Sample	Valid re- sults / measured points	Median of $\varepsilon'_{r,eff}$	Average of $\varepsilon'_{r,eff}$	Standard deviation of $\varepsilon'_{r,eff}$	Minimum of $\varepsilon'_{r,eff}$	Maximum of $\varepsilon'_{r,eff}$
S1U_6460_b	100/100	5.18	5.11	0.35	4.09	6.12
S2U_6460_b	97/100	5.88	5.78	0.58	4.20	6.77
S1U_5520_b	97/100	5.49	5.38	0.81	3.28	7.58
S2U_5520_b	92/100	5.03	5.15	0.54	4.12	6.96
S1U_4420_b	95/100	6.17	6.05	0.55	4.61	6.82
S2U_4420_b	98/100	5.65	5.60	0.78	4.05	7.43

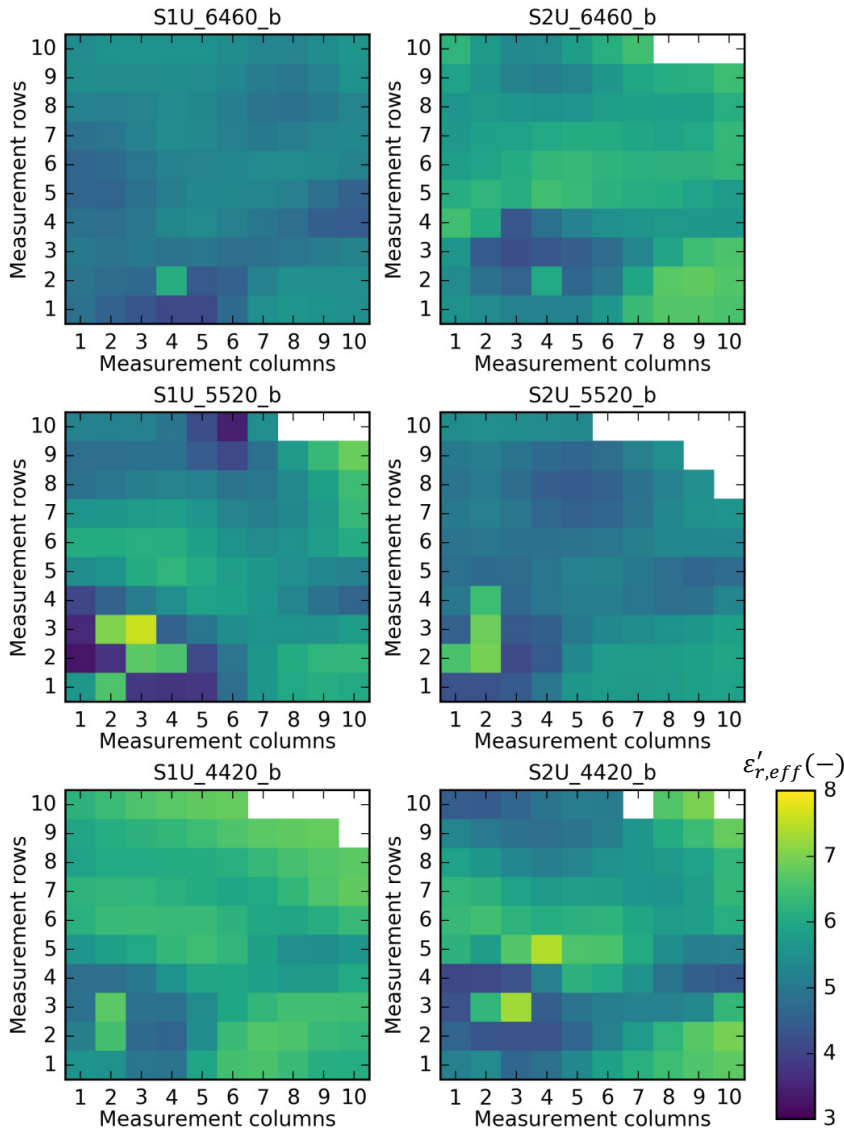


**Figure 34.** Real part of effective permittivity obtained with the VNA scanning of selected asphalt samples from Yläne.

The real part of the effective permittivity measured with microwave radar is on average lower than values obtained with transmission measurements when results from Yläne are examined. In road measurements more of the lower permittivity values are appearing. One reason for this might be that the radar measurement is influenced more of the material properties near the surface whereas the transmission method averages the whole sample volume under the antenna illuminating area. The asphalt surface is always more or less uneven and there might be small holes which have an effect on the permittivity readings.

All Yläne samples have air voids less than 3.1 % and the average is 1.9 % with the dry method (Table 5). This would indicate in the context of NDT with radar that variations in permittivity results should be small too. It was, however, observed that the difference in maximum and minimum of  $\varepsilon'_{r,eff}$  is several units, for both microwave radar and transmission measurements.

## 4.2 Permittivity and permeability of studied rock specimens

### 4.2.1 Dielectric permittivity results

The dielectric permittivity of six rock specimens was measured with a cavity resonator based set-up (see Section 3.3.2). The relative permittivity results and the sample manufacturing dimensions are presented in Table 8. The specimens had an average diameter  $D$  of 11.50 mm and thickness  $d$  of 4.98 mm. The real part of the relative permittivity varies from 5.90 to 6.15, and the imaginary part from 0.022 to 0.046. The average of  $\varepsilon'_r$  is 6.01 and the average of  $\varepsilon''_r$  0.031. The standard deviation of  $\varepsilon'_r$  was calculated to be 0.089. All measured values of  $\varepsilon'_r$  and  $\varepsilon''_r$  are quite close to each other, which is not an unexpected result as all samples were drilled from a rather small volume of rock. The measured average relative permittivities are also well in line with previous observations. Relative permittivity results of the same amphibolite-facies metavolcanic rock type with intermediate composition was studied by Olkkonen et al. (2015). In this rock type, the main minerals are plagioclase and hornblende amphibole. The relative permittivity of plagioclase feldspar series varies from 5.39 to 7.24 (Keller 1988). In this study, the emphasis was more on the permeability measurements which are presented next.

**Table 8.** Permittivity results obtained with the cavity resonator set-up and specimen dimensions.

Specimen	$D$ (mm)	$d$ (mm)	$f_c$ (GHz)	$\varepsilon'_r$ (-)	$B$ (MHz)	$Q_r$ (-)	$\varepsilon''_r$ (-)
A1	11.45	4.92	10.395	5.94	39	267	0.022
A2	11.30	4.90	10.373	6.15	77	135	0.046
A3	11.50	4.96	10.250	6.09	63	163	0.037
A4	11.60	5.36	10.198	5.90	48	212	0.028
A5	11.72	4.91	10.227	5.94	53	193	0.031
A6	11.40	4.80	10.455	6.01	42	249	0.024
<b>Average</b>	11.50	4.98	10.316	6.01	54	203	0.031

### 4.2.2 Magnetic permeability results

The magnetic permeability measurement set-ups were described in Section 3.3.3. The measured real part of relative permeability and estimated resonator quality factor change  $Q/Q_0$  in each test frequency has been summarized in Table 9. The highest  $\mu'_r$  was 1.031 for specimen A5 at 120 MHz, while the average of the real part of the relative permeability at different frequencies was 1.02. The

reference value  $Q_0$  is taken from the empty coil configuration. At all three frequencies it was 100-130 which is typical of the simple construction. Because  $\mu'_r$  is already so close to unity, a meaningful definition of the minimal magnetic losses is not possible here. Although rock specimens were sawn in three different orthogonal directions, no variations were observed between them. Two consecutive samples (A1-A2, A3-A4 and A5-A6) were sawn into the same direction close to each other.

**Table 9.** Relative permeability of rock specimens measured with the LC resonators at three different frequencies.

	120 MHz		250 MHz		500 MHz	
Specimen	$\mu'_r$ (-)	$Q/Q_0$ (-)	$\mu'_r$ (-)	$Q/Q_0$ (-)	$\mu'_r$ (-)	$Q/Q_0$ (-)
A1	1.026	1.07	1.020	1.25	1.016	0.88
A2	1.022	0.99	1.015	1.20	1.013	0.93
A3	1.022	0.99	1.020	1.14	1.016	0.91
A4	1.020	0.99	1.023	1.09	1.018	0.86
A5	1.031	0.98	1.018	1.09	1.019	0.90
A6	1.024	0.99	1.026	1.09	1.021	0.87

In Fig. 35, the measured permeability values are plotted as a function of the frequency. The highest real part of relative permeability is measured with the lowest frequency for most specimens. However, specimens A1 and A3 behave in a different way. In general, the variation in permeability results between different specimens is larger compared with the variation between different frequencies. In this study, the frequency range is relatively small, so that no large variations were expected between different frequencies.

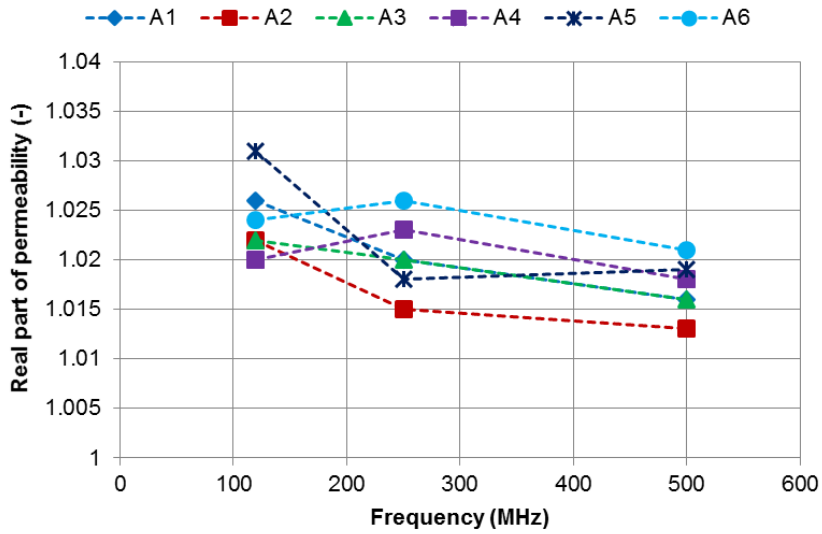


**Figure 35.** Real part of relative permeability of rock specimens A1-A6 measured at frequencies 120 MHz, 250 MHz and 500 MHz.

If the magnetic volume susceptibility is calculated from the magnetic permeability (Eq. 18) for the highest measured value, 1.031, it results to the  $\chi_m$  of 0.031 SI. Similar volume susceptibility values have been measured from intermediate volcanic rocks according to (Airo & Säävuori 2013). Although, the measured magnetic permeability values are slightly higher than 1, these test items can be considered being of low permeability type. Therefore, it can be estimated that the radar applications in similar circumstances can directly utilize impedance and reflection computation based on the permittivity alone (Eq. 31).

### 4.3 Effective permittivity results of granular specimens

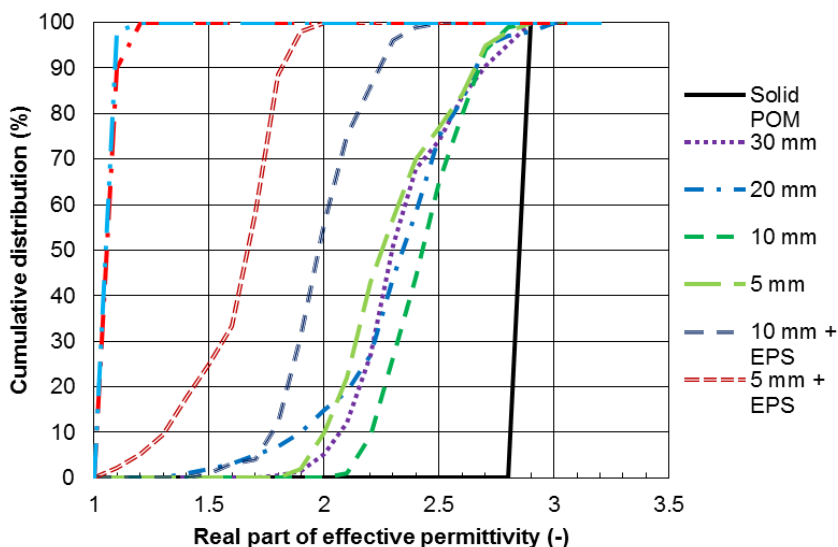
#### 4.3.1 Effective permittivity results of plastics

The effective permittivity results of different plastic granules and solid POM plate are presented in Table 10. The measurements were conducted with the transmission configuration explained in Section 3.4.3. In general, granular specimens have lower average effective permittivity than the solid specimen, which is in accordance with the intuition. When the proportion of air is increasing in the specimen, the effective permittivity should decrease as the permittivity of air is 1. Granularity of specimens has an increasing effect on the standard deviation and the range of effective permittivity. The reason for this is that volume of air and solid materials can vary from one measurement point to another when the material grain size is increasing compared with the antenna footprint and the wavelength.

**Table 10.** Statistics of effective permittivity results of plastics.

Specimen	Valid results / measured points	Median of $\epsilon'_{r,eff}$	Average of $\epsilon'_{r,eff}$	Standard deviation of $\epsilon'_{r,eff}$	Minimum of $\epsilon'_{r,eff}$	Maximum of $\epsilon'_{r,eff}$
Sawing waste A	100/100	1.06	1.06	0.02	1.04	1.11
Sawing waste B	100/100	1.08	1.09	0.02	1.06	1.14
5 mm + EPS	96/100	1.68	1.62	0.20	1.07	1.94
10 mm + EPS	100/100	1.99	1.99	0.17	1.49	2.43
5 mm	100/100	2.25	2.29	0.24	1.82	2.90
10 mm	98/100	2.45	2.43	0.18	2.07	2.88
20 mm	100/100	2.36	2.31	0.30	1.39	2.96
30 mm	190/225	2.30	2.34	0.24	1.74	2.88
Solid POM	100/100	2.84	2.84	0.01	2.82	2.86

Fig. 36 shows effective permittivity results of plastic granules and solid plate as cumulative distributions. In this way, it is easier to display the variation of the permittivity results and to compare the effect of granularity to the solid material results. Again similar notes can be drawn as from the data in Table 10. The solid plate results over the specimen vary only slightly, the standard deviation of  $\epsilon'_{r,eff}$  being 0.01. Whereas granular specimens have more varying results, the standard deviation of  $\epsilon'_{r,eff}$  rising up to 0.30. The cumulative distributions of granules have gradual bends but the solid plate distribution is almost a straight line. The deviation in the 'Sawing waste' specimens A and B is also minor, but these samples can almost be considered as air, because the  $V_a$  is over 95 % (Table 4).

**Figure 36.** Scanned effective permittivity values for solid POM plate and plastic granules of different sizes presented as cumulative distributions.

The total number of measured points compared to the amount of valid results is also listed in Table 10, in addition to other statistics. Up to 30 measurement points had to be excluded from the data analysis, because the phase information obtained with the VNA showed nonlinear behaviour and reliable calculation of effective permittivity was, therefore, inconceivable. Mostly, this concerns 30 mm granules. The results also indicate that for many granule sizes, some of the effective permittivity results exceed the relative permittivity of the solid POM plate. At first, this is an unexpected result. However, it must be noted that especially the 10-30 mm cubes are about the same size as the wavelength in the POM for frequencies 7-17 GHz (see Table 1). Because of the relatively small wavelength, individual granules start to affect the effective permittivity results. In consequence, the EM waves are reflected from the individual cube surfaces and causing further reflections. This can be observed in increasing permittivity values. In the case when these multiple reflections occur, the radar signal path is actually longer and therefore the measured group delay larger. But the true signal path cannot be determined, and instead the smaller sample thickness is used in Eq. (29).

The median of effective permittivity and air voids of plastic specimens are compared in Fig. 37. The error bars for the air void content were calculated based on the minimum and maximum of box dimensions, and the range of effective permittivity results based on the standard deviation. Furthermore, the permittivity mixing models are plotted as dashed lines. The modelled values were obtained using Eqs. (23-25), and using relative permittivity of 2.84 for the solid POM, and 1 for air. Analysing the results in Fig. 37, it must be acknowledged that the air void content was determined using the total box volume, whereas the permittivity was measured from the smaller area.

It seems that the linear model (Eq. 24) gives better match to our results than the complex refractive index model (CRIM) (Eq. 25) or Maxwell Garnett (Eq. 23), as the results have a linear trend. However, all the measured values appear to be shifted to the right relative to the models. This might be related to the method of determining air voids from the dimensions. This methodology seems to overestimate the volume of air, and it only provides the total volume of air for the entire specimen. However, the effective permittivity result is affected by the smaller volume between the antennas, which is related to the illumination area of the antenna.



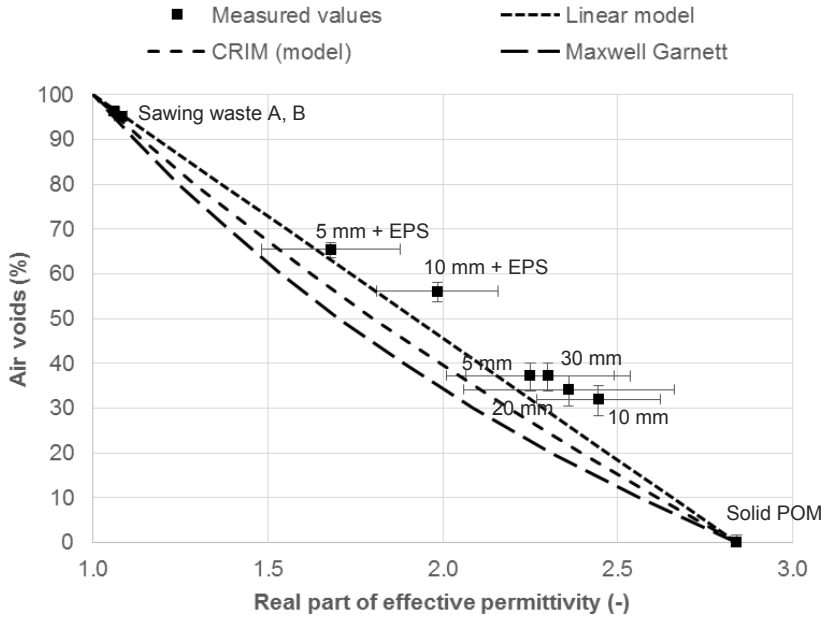


**Figure 37.** Permittivity results of solid POM plate and POM granules of different sizes compared to the volume of air in the boxes. Theoretical models are presented as dashed lines.

**4.3.2 Effective permittivity of asphalt aggregate and filler specimens**

Some of the asphalt raw materials (Section 3.4.1) were also measured with the VNA transmission configuration (Section 3.4.3). Effective permittivity results of the aggregate blend and the filler specimens (see Fig. 25) are presented in Table 11. The standard deviation of effective permittivity is much smaller for the filler, 0.08, compared to the aggregate blend, 0.94. Also, the range of the permittivity values of the aggregate blend is remarkably large, 3.2-8.1. In (Olkkonen et al. 2015), the relative permittivity of metavolcanic rock with intermediate composition was measured with different measurement configuration. For this type of rock, the average of the relative permittivity was 6.21 and the standard deviation 0.20 (Olkkonen et al. 2015), with the VNA transmission method corresponding the measurement set-up in this study. The resonator based measurement which was presented in Section 4.2.1 provided 6.01 for the average of  $\epsilon'_r$ . Comparing the range with the material relative permittivity of 6.2, some of the measured values seems to be too high. However, it must be recalled that the rock material itself is not homogenous. The rocks are actually composites of minerals, and the variation in rock mineralogy can also produce variations in measured effective permittivities.

**Table 11.** Effective permittivity results of raw materials

Specimen	Valid results / measured points	Median of $\epsilon'_{r,eff}$	Average of $\epsilon'_{r,eff}$	Standard deviation of $\epsilon'_{r,eff}$	Minimum of $\epsilon'_{r,eff}$	Maximum of $\epsilon'_{r,eff}$
Aggregate blend	100/100	4.42	4.52	0.94	3.17	8.12
Filler	100/100	2.82	2.80	0.08	2.50	2.95

It was estimated from the box dimensions and the mass that the air void content for the aggregate blend is 46 %, and for the filler specimen 62 %. Linear model (Eq. 24) can also be tested for back-calculating the relative permittivity of solid materials if air voids and effective permittivities have been measured. For the aggregate blend, we get 7.3 of the relative permittivity of the rock material, and 5.8 for the filler relative permittivity, using the median of  $\epsilon'_{r,eff}$ . Both are fairly reasonable values, but the rock relative permittivity of 7.3 seems to be an over-estimate compared with the measured values.

In Fig. 38, effective permittivity results are presented as maps for the aggregate blend and the filler specimens. The effect of larger grain size can be seen by comparing the filler and aggregate results as the permittivity change from one measurement point to another is greater for the coarser aggregate grains. This is partly caused by different volume portions of grains and air. Because of the fine particle size of the filler, the air void content is estimated to vary less across the specimen. Also, the orientation and the shape of individual grains can affect the results. The scattering cross section of the individual grain is different if a top of a grain is facing perpendicularly or in an angle to the incident field. Therefore, the portions of the transmitted and reflected signal can change, which can slightly affect the measured permittivity value. It seems that the very fine particle grain size of the filler specimen is not causing multiple reflections the effective permittivity measurements.

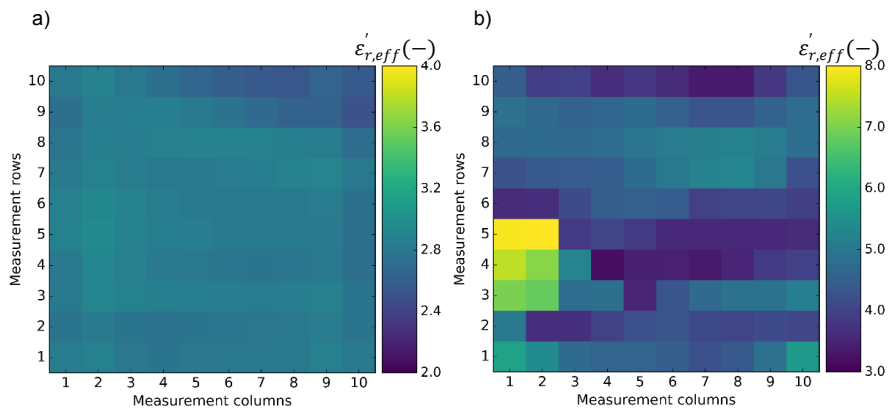


**Figure 38.** a) Effective permittivity scanning results of mineral filler. b) Effective permittivity scanning results of rock aggregate specimen.

4.3.3 Effective permittivity of selected asphalt samples

The median effective permittivity of selected asphalt samples (Section 3.5) is plotted in Fig. 39 against air voids derived from the dry bulk density (Table 5). Linear model (Eq. 24) and CRIM (Eq. 25) are plotted as reference values, using the effective permittivity of 6 for solid material and varying the volume of air. The error bars were marked based on the standard deviation of  $\epsilon'_{r,eff}$  in Fig. 39. The largest standard deviation of  $\epsilon'_{r,eff}$  was 1.4 for a sample from site B.

The measured effective permittivity and air voids do not clearly follow modelled values in Fig. 39, which can be expected as the samples have different mixture types and aggregates. However, it was not expected that the effective permittivity results showed this wide range of values. The effective permittivity results suggest that the permittivity is sensitive to other factors as well, in addition to the volume of air. It is clear that the rock relative permittivity affects the effective permittivity as the results of drilled asphalt samples from different sites vary. In addition, the volume portions of rocks and bitumen is varying from one measurement point to another and this is affecting the effective permittivity as well. Based on Fig. 39, deriving air voids simply from the effective permittivity is not meaningful. Even if a calibration sample is taken to modify the model for calculating air voids, outliers seem to exist making the calibration vulnerable for errors.

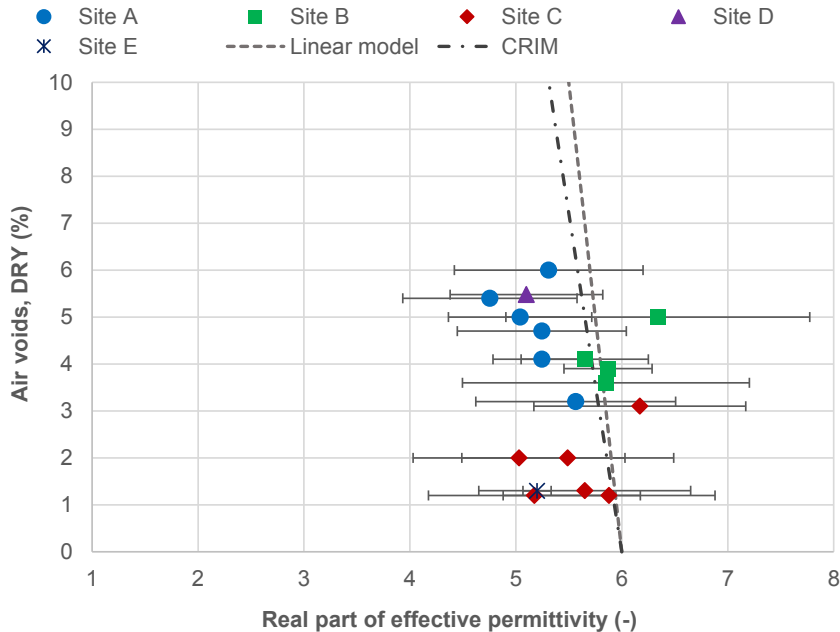


**Figure 39.** Median of the effective permittivity was obtained with VNA scanning and air void results were derived from the dry bulk density. Asphalt sample results from different construction sites are compared against the theoretical (linear and complex refractive index model) effective permittivity values. The error bars of effective permittivity are marked based on the standard deviation.

## 5. Discussion

This study was aimed to address the air void content evaluation of thin granular asphalt pavement layers based on the measured effective permittivity. When the measured effective permittivity is used in non-destructive testing or quality assurance (QA) of composite materials, sources of errors, and on the other hand the sources of natural material variation, should be well recognized and separated. Otherwise, the measured variation can falsely be interpreted as materials with poor quality. Fig. 3 presented different factors causing uncertainty and variation in permittivity measurements. These uncertainties can be related to the measurement instruments and their accuracy, calibration of measurements or material heterogeneity which is actually the studied variation. The following sections discuss the most essential findings of this study which are new information in the context of material evaluation of thin and granular layers with radar.

### 5.1 Reliability and validity of current GPR method in QC of thin overlays

Originally, this study initiated from a theoretical observation that the depth resolution of the 1-2 GHz pulse GPRs is not adequate for correctly measuring the effective permittivity of thin layers (Section 2.8). Although many previous studies (Saarenketo & Scullion 2000; Al-Qadi et al. 2010; Plati & Loizos 2013; Chen et al. 2014; Hoegh et al. 2015) have shown that the compaction evaluation of asphalt pavements with GPR is a successful method, the feasibility in the case of thin layers seems to have been neglected. Only recently, some limitations have been discussed for thin layers. Plati & Loizos (2013) considered the possible effect on permittivity readings when HMA materials change in different layers. However, in their research both HMA layers had the same mixture and the design thickness of 120 mm, and they observed only small changes in permittivities acquired with 1 and 2 GHz GPR systems.

In Finland, the GPR method is, however, applied as QC/QA for wearing course which might have the thickness of approximately 40 mm. Furthermore, the HMA mixture type and rock aggregate origin might vary in different layers as the wearing course should be resistant to abrasion due to the studded winter tires for example. Permittivity properties of different rock types can be considerably dissimilar and, therefore, a reflecting surface may occur between distinct layers. A deeper layer boundary might produce a reflection that interferes with

the surface reflection. For very thin overlays, even the pulse from the 2 GHz GPR is not short enough to separate these two reflections from the pavement surface and from the successive layers.

One of the key aspects in this study was the evaluation of the measurement accuracy and precision with respect of material variation. A major concern of radar systems is related to the measurement of power. This topic was evaluated in Section 2.7.3, which discussed the reflection measurement principle. It was estimated that even if the radar electronics are considered to be of good quality, the power measurement uncertainty can be of the order of 0.5 dB. This can lead to the 0.5 unit difference with the nominal effective permittivity of 5. Similar observations were made by Fauchard et al. (2015) as they concluded that the accuracy of a commercial 2 GHz GPR is not adequate to estimate the compaction of asphalt pavements. Moreover, the relative permittivity measured with the GPR is usually presented with one decimal accuracy. Considering the precision and inaccuracy of GPR systems in measuring relative permittivity from the surface reflection, it seems that the 0.1 accuracy is an overestimation.

When the relative permittivity is calculated from the surface reflection, a calibration signal is needed as well (Eq. 31). The calibration material is usually chosen to be conductive such as metal. This is challenging for the radar electronics as the calibration is done at the very end of dynamic range. Components are not necessarily linearly behaving and calibrating them on the limit of the performance capability may lead to inaccurate measurement results. The magnitude of this effect is, however, dependent on exact components and is, therefore, difficult to estimate quantitatively.

Accounting for these previously presented observations, namely the inadequate depth resolution and power measurement inaccuracy, the reliability of the relative permittivity measured with GPR is questionable in terms of QC/QA of thin overlays. The further question is if similar problems exist in other GPR applications. A similar application is for instance the layer thickness evaluation. Usually, the thickness evaluation concerns thickness of the entire bound pavement structure. In that case, the thickness is considerably larger than 40-50 mm and the depth resolution might be good enough with the 1 GHz central frequency as well. In practical applications naturally, the expected layer thickness needs to be compared with the depth resolution of the GPR available using Eqs. (47-48). Fauchard et al. (2015) stated, that although the compaction evaluation with a commercial 2 GHz GPR antenna is not reasonable, the drift of the GPR system does not destroy the thickness estimation. They calculated the error to be 3 % which results in calculated value of 4.85 cm for the 5 cm thick layer. Zhao & Al-Qadi (2016) recently reported the thickness estimation error to be only 5 mm for layers thicker than 64 mm. They applied a commercial stepped frequency array equipped with 200 MHz - 3 GHz span and the common midpoint method (CMP). Even with this GPR system, it was noticed that accurate thickness estimates could not be achieved for thin layers.

Previously in this section, the air void content evaluation of thin asphalt layers is discussed from the radar measurements point of view. Next, the aim is to briefly look into the mixing models which can be used to estimate the volumetric

proportions of materials (Sihvola 1999; Leng et al. 2011; Fauchard et al. 2013). In Fig. 39, the linear model (Eq. 24) and CRIM (Eq. 25) were plotted as dashed lines, using the effective permittivity of 6 for solid material and varying the volume of air. The effective permittivity corresponding to 10 % air voids is 5.5 with the linear model, and 5.31 with the CRIM. Moreover, 1 % increase in air voids corresponds to 0.05 unit decrease in effective permittivity with the linear model, and approximately 0.07 unit decrease with CRIM (Fig. 39). When the average air voids of SMA is considered for example, air voids should remain between 2 and 5 % (PANK 2011). This means that with GPR the relative permittivity difference that needs to be correctly measured is around 0.05 units. Considering the power measurement uncertainty alone, the precision of radars is not good enough for measuring the effective permittivity of the pavement from the surface reflection. The same conclusion was suggested based on the error analysis of the Eq. (31) presented in Section 2.7.3. Furthermore, it can be concluded that estimation of air voids with traditional 1-2 GHz pulse radars is not a reliable method for the quality assurance of thin asphalt pavements.

## 5.2 Implications of increasing the depth resolution capabilities

To overcome problems due to the limited depth resolution of traditional 1-2 GHz GPR frequencies, a radar with increased depth resolution was needed. As this study was aimed to address applying microwave frequencies in NDT of thin pavement layers, the first solution was to develop a radar with improved depth resolution capabilities. A novel radar assembly was presented in (Huuskonen-Snicker et al. 2015). The introduced radar employs swept continuous wave principle from 12 to 18 GHz with 256 frequency steps. By applying the Eq. (48), the 6 GHz bandwidth and the relative permittivity of 5 results the depth resolution to be better than 1.5 cm. This is a considerable improvement compared to the depth resolution of the 1 GHz pulse GPR, which is at very most 3 cm with the relative permittivity of 5 (Eq. 47). In principal, the corresponding 6 GHz bandwidth can be achieved at slightly lower frequencies as well, such as from 2-8 GHz, but in terms of radar assembly it is not an affordable choice. Therefore, the chosen frequency range was 12-18 GHz.

It was anticipated that employing this high frequencies, 12-18 GHz, might introduce new problems due to the asphalt granularity, which was observed in first road tests. The new microwave radar was tested on different road pavements and results of one test site were presented in Section 4.1.1. The calculated effective permittivities showed a broad range of values. Effective permittivities ranged from close to 1 to over 7. The average of the effective permittivity was 3.14-4.70, and the standard deviation 0.61-0.98 (Table 6). Usually, the variation in effective permittivity results with traditional GPRs is less than what was found with the microwave radar. The granularity of asphalt certainly becomes an issue with these higher frequencies. It must be noted that the individual rock pieces have the nominal grain size reaching up to 16 or even 22 mm (PANK 2011), depending on the asphalt mixture type. If now the depth resolution is of

the same magnitude, it means that the medium cannot be assumed homogeneous. This might explain the wide range observed in permittivity values because in one measurement point the measurement volume might consist mostly of rock material and in another the volume of bitumen or air might be increased.

### 5.3 Implications of permittivity and permeability variations in rocks

Permittivity measurements in laboratory were carried out when the first tests with the new microwave radar revealed more variation in effective permittivity values than was expected based on the theoretical mixing models. As aggregates are the main volumetric component in the asphalt mix, their relative permittivity creates the basic level for the effective permittivity of the total asphalt mix. Therefore, the relative permittivity of a certain rock type was measured, and aggregated sample of the same rock type was studied in addition. Even for the relatively homogenous rock specimens and small sample volume, the real part of the relative permittivity was observed to vary from 5.90 to 6.15 (Table 8). The mix of air and rocks of same rock type had the real part of the relative permittivity from 3.17 to 8.12 (Table 11).

The measured relative permittivity values of rocks do not include the variation from diverse mineralogical compositions of different rock types. It is possible that the rock type changes in a quarry or veins with distinct mineralogical compositions occur in the host rock, such as pegmatite veins in darker, mafic type of rock. The  $\epsilon'_r$  of pegmatite rock specimens were measured in (Olkkonen et al. 2015), which reported the average of  $\epsilon'_r$  to be 4.5 and the standard deviation 0.05. Compared to the real part of relative permittivity close to 6, which was measured in this study, a small difference in volumetric portions of different rock types can evidently lead to changes in the measured effective permittivities of asphalt. Volumetric portion of rock materials in asphalt can exceed 80 %. Nowadays, when the tendency is to use more and more of recycled materials in asphalt too, the origin of rock aggregates can be diverse. This might result in effective permittivity variations along the measured road section even when the air void content would remain constant.

The rarer source of uncertainty in permittivity measurements is the possible magnetic behaviour of rock aggregates due to the certain magnetic minerals in rocks (Keller 1988; Klein & Santamarina 2000). To exclude this possible phenomena in this case, special measurement set-ups were employed to actually measure the magnetic permeability and dielectric permittivity of rock specimens independently from each other. The highest measured  $\mu'_r$  was 1.031 at frequency of 120 MHz and the average of  $\mu'_r$  at different frequencies was 1.02 (Table 9). In conclusion, the magnetic permeability can be neglected in permittivity calculation and applying of Eq. (31) without the permeability terms is valid (Ramo & Whinnery 1956).

Observations of rock permittivity variations add another source of uncertainty in quality control of thin pavement layers. In practical radar applications, the

permittivity variation resulting from aggregates needs to be identified and separated from the air void changes. This is a challenge for radar measurements as the relative permittivity variation of rocks can be substantially larger than that of changing air voids. Previously, it was estimated that 1 % change in air voids decreases the effective permittivity of asphalt by 0.05 units. In comparison, the standard deviation of  $\varepsilon'_r$  was 0.09 for rock specimens in Section 4.2.1.

## 5.4 Implications of grain size

The scanned effective permittivity of the rock aggregate blend interestingly exceeded the relative permittivity of the studied rock type in some measurement points (Fig. 38b). The maximum of  $\varepsilon'_{r,eff}$  was 8.12 (Table 11), which in theory could be the relative permittivity of some rock types. Therefore, similar scanning tests were conducted with granular specimens but now with homogenous materials (Section 4.3.1). Despite the homogenous material, the reliable calculation of the effective permittivity was impossible in some measurement points because the measured phase behaved non-linearly. The largest amount of measurement points that needed to be excluded was from the specimen with 30 mm granules (Table 10).

Three possible explanations were derived for these observations. Water inside porous asphalt samples, magnetic effect from the aggregates or the large grain size of aggregates compared to the applied frequencies can in theory increase the observed effective permittivity. As the same phenomena was observed with dry homogenous and non-magnetic materials, the only possible explanation is that the grain size becomes comparable to applied wavelengths. The EM signal might be reflected from the individual cube surfaces and causing further reflections. Then, the actual signal path is longer than the sample thickness used in Eq. (29).

The air voids and the mean  $\varepsilon'_{r,eff}$  of asphalt specimens did not clearly correlate with the studied mixing models in Fig. 39. Benedetto & De Blasiis (2010) have summarized studies which have reported weak correlations between air voids and relative permittivity of asphalt mixes and subgrades. When mixing models are applied in compaction evaluation, it is often assumed that all the variation is related to changing amount of air voids. But the wide range in measured effective permittivity values suggests that this is not the case. In asphalt mix, the volumetric portions of bitumen and aggregates can slightly change as well (see for example Nevalainen & Pellinen 2016). These changing volumetric portions, in addition to relative permittivity variation of rocks, should be able to differentiate from the impact of changing air void content. The question remains that how this could be achieved.

The wavelength ranges from 7 mm to 17 mm when the material relative permittivity is, for instance, 6 and frequencies are from 7 to 17 GHz (Eq. 22). Comparing the wavelength with the rock aggregate sizes indicates that the wavelength is of the same order of the grain size (see Fig. 26). This implies that the basic assumption of applying electromagnetic mixing models (Sihvola 1989),



namely homogenous media, is not valid. In order to fulfil this assumption, wavelengths should be much larger than the diameter of individual grains. From Eq. (22) it can be derived that approximately under 4 GHz, and the relative permittivity being 5, the wavelength is approximately 30 mm. Therefore, the applied frequencies should be lower than 4 GHz to have the long enough wavelength. Frequency range from 0.4 to 6 GHz was adopted by Fauchard et al. (2015), where the designed thickness of the first layer was 6 cm, but the maximum grain size was not reported. In their study the measurement set-up included laboratory scale equipment for producing the rather large frequency range at low centre frequency. In our study, one of the aims was to develop an affordable radar system for road testing.

Finally, the applied frequencies should be considered bearing the sufficient depth resolution for thin layers in mind. A 4 GHz frequency span seems to produce good enough depth resolution for approximately 4 cm layers (Eqs. 47-48). Further studies should be conducted to evaluate the applicability of frequencies around 4 GHz in NDT of thin pavement layers. Nevertheless, it must be noted that the appropriate frequency range selection is only one aspect in reliable QC/QA of thin pavement layers. As was discussed previously, the permittivity variation of rock aggregates and measurement accuracy of permittivity from the surface reflection seem to be serious limitations.

## 5.5 Issues related to polarization of electromagnetic wave

Polarization of electromagnetic waves has not been discussed previously in this work although it should be acknowledged when designing different measurement set-ups and analysing their results. During this study, it was realized that especially when granular and heterogeneous materials are studied the polarization might become an issue. The polarization refers to the orientation of the field vectors of plane waves (Ramo & Whinnery 1956). Sinusoidal waves can be linearly, circularly or elliptically polarized. When the electric field vector maintains its orientation along a straight line, the electric field is described as linearly polarized.

According to Baker et al. (2007), the polarization of GPR signal actually involves three different concepts: polarization due to antenna construction, polarization due to antenna orientation and depolarization due to target orientation. Antennas transmit polarized waves and many commercial GPRs transmit linearly polarized signals. The microwave radar used in this study was equipped with linearly polarized antennas (Huuskonen-Snicker et al. 2015). The polarization in the microwave radar measurements is along the road surface, i.e. perpendicularly against the signal propagation from the antenna (Fig. 40b). In comparison to propagating EM waves from antennas, a standing wave pattern is formed inside the microwave resonator. Depending on the excited mode or modes, the field inside the resonator is, for example, downwards towards the sample. The field orientation is, therefore, dissimilar in radar and also in the

transmission measurements with the waveguide antennas in comparison to resonator method (Fig. 40a). If the studied material is anisotropic, the measured permittivity is dependent on the direction of the electric field.

Polarization due to antenna orientation includes positioning transmitting and receiving antennas in relation to each other, as well as in relation to the survey line direction. Orlando & Slob (2009) have used a GPR system, which was equipped with 2 GHz dipoles in a rectangular arrangement. The GPR system they applied can be used to receive the electric field in four different configurations at the same time and position. Different antenna orientations have as well been exploited by Hugenschmidt & Kalogeropoulos (2009) to reduce the directionality of GPR in the concrete retaining wall survey. Radzevicius & Daniels (2000) have presented in a comprehensive study how reflected GPR signal from a cylinder may be depolarized due to target orientation relative to antennas.

Practical implications that may follow from different field polarizations are related to the permittivity results of asphalt. The different orientations of electric field vectors is one possible explanation why resonator measurements in comparison to radar or transmission measurements produced slightly different permittivity values. However, the exact effect is not known as measurements were not particularly planned to answer this question.

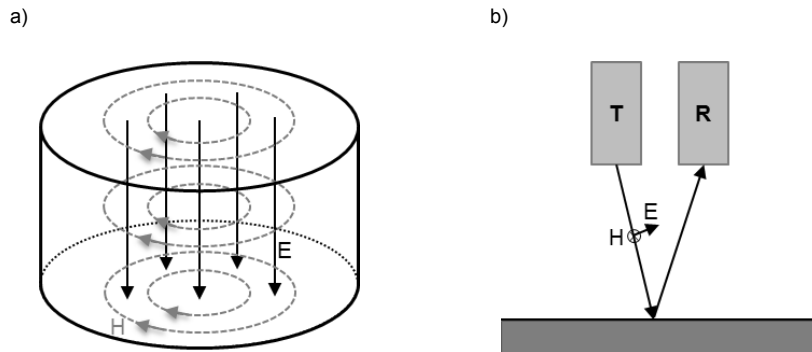


**Figure 40.** a) A schematic figure of the field pattern inside the circular cavity resonator (magnetic field lines as grey dashed lines and electric field lines as black lines. b) The polarization in the microwave radar measurements is along the road surface, i.e. perpendicularly against the signal propagation from the antenna.



## 6. Conclusions

The aim of this study was to evaluate if GPR, or microwave technologies in general, are feasible in the air void content estimation of thin asphalt layers. Based on this study, the following preconditions can be formulated which ensure successful application of radar in QC/QA of asphalt pavement:

- The depth resolution of the available radar system needs to be compared with the thickness of the studied layer. If the depth resolution is not good enough to truly separate deeper reflections from the surface reflection, the obtained relative permittivity of the top layer may be incorrect.
- The accuracy and precision of the radar system needs to be evaluated compared with the aimed accuracy of the measurement. For example, the insufficient power measurement precision due to the radar electronics produces an error to the calculated relative permittivity from the surface reflection amplitudes.
- The applied wavelengths should be compared with the aggregate grain sizes. When the electromagnetic mixing models are exploited to calculate the air void content of the asphalt based on the measured effective permittivity, the basic assumption is that the distinct pieces of materials are small relative to the applied wavelength. In this study, violating this assumption produced the effective permittivity values of the mix exceeding the material relative permittivity.
- The successful application of electromagnetic mixing models requires also knowledge on the relative permittivity of each component in the mixture and their volumetric proportions. This means that the relative permittivity of the aggregates needs to be analysed. As aggregates from different origins may be used in the same asphalt mix, the reliable estimation of the permittivity variations due to the aggregates can become an issue.
- In rare cases, the magnetic permeability of rock aggregates can have an effect of the relative permittivity measurements of the asphalt.

- More common problem is water inside the asphalt pavement increasing the measured effective permittivity.

If preconditions presented above are satisfied, radar methods can be applied in the air void content estimation of thin asphalt layers. However, as the GPR systems are currently applied in Finland according to PANK-4122, preconditions presented here are not fulfilled. The most profound problems are related to the applied pulse widths compared with the layer thicknesses. In addition, the relative permittivity variation of rocks cannot be controlled as the source of aggregates may be unknown.

# References

- Airo, M.-L., and Säävuori, H. (2013). Petrophysical characteristics of Finnish bedrock : Concise handbook on the physical parameters of bedrock. Espoo: Geological Survey of Finland. 33 p. Report of Investigation 205. Available at: <https://www.gtk-kauppa.fi/products/view/14359>.
- Al-Qadi, I. L., Leng, Z., Lahouar, S., and Baek, J. (2010). In-place hot-mix asphalt density estimation using ground-penetrating radar. *Transportation Research Record*. Vol. 2152. pp. 19-27.
- Annan, A. P. (2003). Ground Penetrating Radar: Principles, Procedures & Applications. Mississauga, Canada: Sensors & Software Inc.
- Annan, A. P. (2009). Electromagnetic principles of ground penetrating radar. In: Jol, H. M. (ed.) Ground Penetrating Radar Theory and Applications. Amsterdam: Elsevier. pp. 41-72.
- Baker, G. S., Jordan, T. E., and Talley, J. (2007). An introduction to ground penetrating radar (GPR). In: Baker, G. S., and Jol, H. M. (eds.) Stratigraphic Analyses Using GPR. Boulder: Geological Society of America. pp. 1-18. Special Paper 432.
- Balanis, C. A. (1989). Advanced Engineering Electromagnetics. New York: John Wiley & Sons. 981 p.
- Barrile, V., and Pucinotti, R. (2005). Application of radar technology to reinforced concrete structures: a case study. *NDT & E International*. Vol. 38:7. pp. 596-604.
- Benedetto, A., and De Blasiis, M. (2010). Applications of Ground Penetrating Radar to Road Pavement: State of the Art and Novelties. In: Huang, B., Tutumluer, E., Al-Qadi, I. L., Prozzi, J., and Shu, X. (eds.) Paving Materials and Pavement Analysis. Shanghai. 3-5.6.2010. GeoShanghai International Conference 2010. pp. 412-419.
- Benson, A. K. (1995). Applications of ground penetrating radar in assessing some geological hazards: examples of groundwater contamination, faults, cavities. *Journal of Applied Geophysics*. Vol. 33:1. pp. 177-193.
- Brunett, J. D., Aryanfar, F., Entesari, K., and Yang, T. (2003). The effects of ground permittivity and surface roughness on multi-path measurements at K-band. Antennas and Propagation Society International Symposium, 2003. IEEE. Columbus, OH, USA. 22-27.6.2003. pp. 408-411.
- Bruschini, C., Gros, B., Guerne, F., Pièce, P-Y., and Carmona, O. (1998). Ground penetrating radar and imaging metal detector for antipersonnel mine detection. *Journal of Applied Geophysics*. Vol. 40:1-3. pp. 59-71.
- Bungey, J. H. (2004). Sub-surface radar testing of concrete: a review. *Construction and Building Materials*. Vol. 18:1. pp. 1-8.
- Cassidy, N. J. (2008). Frequency-dependent attenuation and velocity characteristics of nano-to-micro scale, lossy, magnetite-rich materials. *Near Surface Geophysics*. Vol. 6:6. pp. 341-354.
- Cassidy, N. J. (2009). Electrical and magnetic properties of rocks, soils and fluids. In: Jol, H. M. (ed.) Ground Penetrating Radar Theory and Applications. Amsterdam: Elsevier. pp. 41-72.

- Cassidy, N. J., and Millington, T. M. (2009). The application of finite-difference time-domain modelling for the assessment of GPR in magnetically lossy materials. *Journal of Applied Geophysics*. Vol. 67:4. pp. 296-308.
- Cassidy, N. J., Eddies, R., and Dods, S. (2011). Void detection beneath reinforced concrete sections: The practical application of ground-penetrating radar and ultrasonic techniques. *Journal of Applied Geophysics*. Vol. 74:4. pp. 263-276.
- Chen, D.-H., Hong, F., Zhou, W., and Ying, P. (2014). Estimating the hotmix asphalt air voids from ground penetrating radar. *NDT & E International*. Vol. 68. pp. 120-127.
- Clark, D. A. (1997). Magnetic petrophysics and magnetic petrology: aids to geological interpretation of magnetic surveys. *AGSO Journal of Australian Geology & Geophysics*. Vol. 17:2. 83-103.
- Daniels, D. J. (2004). Ground Penetrating Radar. 2nd ed. London: IEE. 726 p.
- Dolukhanov, M. (1971). Propagation of radio waves. Moscow: MIR Publishers. pp. 41-43.
- Doré, G., and Zubeck, H. K. (2009.) Cold regions pavement engineering. Reston, VA: ASCE Press. 416 p.
- Eyraud, C., Geffrin, J. M., Litman, A., and Tortel, H. (2015). Complex Permittivity Determination From Far-Field Scattering Patterns. *IEEE Antennas and Wireless Propagation Letters*. Vol. 14. pp. 309-312.
- Fauchard, C., Li, B., Laguerre, L., Héritier, B., Benjelloun, N., and Kadi, M. (2013). Determination of the compaction of hot mix asphalt using high-frequency electromagnetic methods. *NDT & E International*. Vol. 60. pp. 40-51.
- Fauchard, C., Beaucamp, B., and Laguerre, L. (2015). Non-destructive assessment of hot mix asphalt compaction/ density with a step-frequency radar: case study on a newly paved road. *Near Surface Geophysics*. Vol. 13:3. pp. 289-297.
- Gader, P. D., Mystkowski, M., and Zhao, Y. (2001). Landmine detection with ground penetrating radar using hidden Markov models. *IEEE Transactions on Geoscience and Remote Sensing*. Vol. 39:6. pp. 1231-1244.
- Geological Survey of Finland. Finnish bedrock 1:200 000. [Cited 26 April 2016]. Available at: <http://gtkdata.gtk.fi/Maankamara/index.html>.
- Gibbard, P. L., Pasanen, A. H., West, R. G., Lunkka, J. P., Boreham, S., Cohen, K. M., and Rolfe, C. (2009). Late Middle Pleistocene glaciation in East Anglia, England. *Boreas*. Vol. 38:3. pp. 504-528.
- Hasch, J., Topak, E., Schnabel, R., Zwick, T., Weigel, R., and Waldschmidt, C. (2012). Millimeter-Wave Technology for Automotive Radar Sensors in the 77 GHz Frequency Band. *IEEE Transactions on Microwave Theory and Techniques*. Vol. 60:3. pp. 845-860.
- Hartikainen, A., Pellinen, T., Eskelinen, P., Huuskonen-Snicker, E. (2016a). Algorithm to process the stepped frequency radar signal for a thin road surface application. *Submitted*.
- Hartikainen, A., Pellinen, T., Huuskonen-Snicker, E., Eskelinen, J., and Eskelinen, P. (2016b). Road pavement density evaluation - a case study. 4th International Chinese European Workshop (CEW) on functional pavement design. Delft, Netherlands. 29.6-1.7.2016.
- He, X.-Q., Zhu, Z.-Q., Liu, Q.-Y., and Lu, G.-Y. (2009). Review of GPR rebar detection. Progress in Electromagnetics Research Symposium, PIERS 2009. Beijing. 23-27.3.2009.
- Hiebel, M. (2014). Fundamentals of vector network analysis. 6th ed. München: Rohde&Schwarz.

- Hoegh, K., Khazanovich, L., Dai, S., and Yu, T. (2015). Evaluating asphalt concrete air void variation via GPR antenna array data. *Case Studies in Nondestructive Testing and Evaluation*. Vol. 3. pp. 27-33.
- Holden, J., Burt, T. P., and Vilas, M. (2002). Application of ground-penetrating radar to the identification of subsurface piping in blanket peat. *Earth Surface Processes and Landforms*. Vol. 27:3. pp. 235-249.
- Huang, Y. H. (1993). Pavement analysis and design. Upper Saddle River, New Jersey: Prentice Hall. 805 p.
- Huber+Suhner. RF Coaxial connectors: General catalogue. [Cited 25 April 2016]. Available at: <http://literature.hubersuhner.com/Technologies/Radiofrequency/RFConnectorsEN/?page=171>.
- Hugenschmidt, J., and Loser, R. (2008). Detection of chlorides and moisture in concrete structures with ground penetrating radar. *Materials and Structures*. Vol. 41:4. pp. 785-792.
- Hugenschmidt, J., and Kalogeropoulos, A. (2009). The inspection of retaining walls using GPR. *Journal of Applied Geophysics*. Volume 67:4. pp. 335-344.
- Huisman, J. A., Hubbard, S. S., Redman, J. D., and Annan, A.P. (2003). Measuring soil water content with ground penetrating radar: A review. *Vadose Zone Journal*. Vol. 2:4. pp. 476-491.
- Huuskonen-Snicker, E., Eskelinen, P., Pellinen, T., and Olkkonen M.-K. (2015). A New Microwave Asphalt Radar Rover for Thin Surface Civil Engineering Applications. *Frequenz*. Vol. 69:7-8. pp. 377-381.
- Hänninen, P. (1992). Application of ground penetrating radar and radio wave moisture probe techniques to peatland investigations. Espoo: Geological Survey of Finland. 71 p. Geological Survey of Finland, Bulletin 361. Available at: [http://tupa.gtk.fi/julkaisu/bulletin/bt\\_361.pdf](http://tupa.gtk.fi/julkaisu/bulletin/bt_361.pdf).
- Itoh, T., and Rudokas, R. (1976). New Method for Computing the Resonant Frequencies of Dielectric Resonators. Rome. 14-17.9.1976. 6th European Microwave Conference. pp. 702-706.
- ITT. (1977). Reference data for radio engineers. 6th ed. Indianapolis: Howard W. Sams & Co., Inc. a subsidiary of ITT. pp. 4-30.
- Jamil, M., Hassan, M. K., Al-Mattarneh, H. M. A., Zain, M. F. M. (2013). Concrete dielectric properties investigation using microwave nondestructive techniques. *Materials and Structures*. Vol. 46:1. pp. 77-87.
- Jol, H. M., and Smith, D. G. (1995). Ground penetrating radar surveys of peatlands for oilfield pipelines in Canada. *Journal of Applied Geophysics*. Vol. 34:2. pp. 109-123.
- Kajfez, D., and Guillon, P. (1986). Dielectric resonators. Norwood, MA: Artech House. pp. 174-181.
- Kalogeropoulos, A., van der Kruk, J., Hugenschmidt, J., Busch, S., and Merz, K. (2011). Chlorides and moisture assessment in concrete by GPR full waveform inversion. *Near Surface Geophysics*. Vol 9:3. pp. 277-285.
- Keller, G. V. (1988). Rock and mineral properties. In: Nabighian, M. N. (ed.) *Electromagnetic methods in applied geophysics – theory*, vol. 1. Tulsa: Society of Exploration Geophysics. pp 13-51.
- Klein, K., and Santamarina, J. C. (2000). Ferromagnetic Inclusions in Geomaterials: Implications. *Journal of Geotechnical and Geoenvironmental Engineering*. Vol. 126:2. pp. 167-179.
- Klysz, G., and Balayssac, J. P. (2007). Determination of volumetric water content of concrete using ground-penetrating radar. *Cement and Concrete Research*. Vol. 37:8. pp. 1164-1171.



- Knott, E., Shaeffer, J., and Tuley, M. (1993). Radar cross section. 2nd ed. Norwood, MA: Artech House. pp. 225-267.
- Koppenjan S. (2009). Ground penetrating radar systems and design. In: Jol, H. M. (ed.) Ground Penetrating Radar Theory and Applications. Amsterdam: Elsevier. pp. 73-97.
- Lahouar S. (2003). Development of Data Analysis Algorithms for Interpretation of Ground Penetrating Radar Data. Doctoral thesis. Virginia Polytechnic Institute and State University. Blacksburg, Virginia.
- Lambot, S., Slob, E. C., Van Bosch, I. D., Stockbroeckx, B., Vanclooster, M. (2004). Modeling of ground-penetrating radar for accurate characterization of subsurface electric properties. *IEEE Transactions on Geoscience and Remote Sensing*. Vol. 42:11. pp. 2555-2568.
- Laurens, S., Balayssac, J., Rhazi, J., and Arliguie, G. (2002). Influence of concrete relative humidity on the amplitude of Ground-Penetrating radar (GPR) signal. *Materials and Structures*. Vol. 35:4. pp. 198-203.
- Laurens, S., Balayssac, J., Rhazi, J., Klysz, G., and Arliguie, G. (2005). Non-destructive evaluation of concrete moisture by GPR: Experimental study and direct modeling. *Materials and Structures*. Vol. 38:9. pp. 827-832.
- Lehtinen, M., Nurmi, P. A., and Rämö O. T. (eds.) (2005). Precambrian Geology of Finland: Key to the Evolution of the Fennoscandian Shield. Amsterdam: Elsevier. 736 p. Developments in Precambrian Geology, 14.
- Leng, Z. (2011). Prediction of in-situ asphalt mixture density using ground penetrating radar: theoretical development and field verification. Doctoral thesis. University of Illinois at Urbana-Champaign. Illinois.
- Leng, Z., Al-Qadi, I., and Lauhouar, S. (2011). Development and validation for in situ asphalt mixture density predictions models. *NDT & E International*. Vol. 44:4. pp. 369-375.
- Maierhofer, C. (2003). Nondestructive evaluation of concrete infrastructure with ground penetrating radar. *Journal of Materials in Civil Engineering*. Vol. 15:3. pp. 287-297.
- Maser, K. R., and Scullion, T. (1992). Automated pavement subsurface profiling using radar: case studies of four experimental field sites. *Transportation Research Record 1344*. pp. 148-154.
- Matthaei, G., Young L., and Jones E. (1980). Microwave filters, impedance-matching networks, and coupling structures. Norwood, MA: Artech House.
- Meinel, H. H. (1995). Commercial Applications of Millimeterwaves History, Present Status, and Future Trends. *IEEE Transactions on Microwave Theory and Techniques*. Vol. 43:7. pp. 1639-1653.
- Moore, J. C., Pälli, A., Ludwig, F., Blatter, H., Jania, J., Gadek, B., Glowacki, P., Mochnecki, D., and Isaksson, E. (1999). High-resolution hydrothermal structure of Hansbreen, Spitsbergen, mapped by ground-penetrating radar. *Journal of Glaciology*. Vol. 45:151. pp. 524-532.
- Nakashima, Y., Zhou, H., and Sato, M. (2001). Estimation of groundwater level by GPR in an area with multiple ambiguous reflections. *Journal of Applied Geophysics*. Vol. 47:3-4. pp. 241-249.
- Neal, A. (2004). Ground-penetrating radar and its use in sedimentology: principles, problems and progress. *Earth-Science Reviews*. Vol. 66:3-4. pp. 261-330.
- Nelson, S. O. (2005). Density-permittivity relationships for powdered and granular materials. *IEEE Transactions on Instrumentation and Measurement*. Vol. 54:5. pp. 2033-2040.

- Nesse, W. D. (2011). Introduction to mineralogy. 2nd ed. New York: Oxford University Press. 496 p.
- Nevalainen, N., and Pellinen, T. (2016). The use of a thermal camera for quality assurance of asphalt pavement construction. *International Journal of Pavement Engineering*. Vol. 17:7. pp. 626-636.
- Nyfors, E., and Vainikainen, P. (1989). Industrial microwave sensors. Norwood, MA: Artech House.
- Nyfors, E. (2000) Cylindrical microwave resonator sensors for measuring materials under flow. Doctoral thesis. Helsinki University of Technology, Radio Laboratory. Espoo.
- Olhoeft, G. R., Strangway, D. W. (1974). Magnetic relaxation and the electromagnetic response parameter. *Geophysics*. Vol. 39:3. pp. 302-311.
- Olkkonen, M., Mikhnev, V., and Huuskonen, E. (2012). RF moisture measurement of concrete with a resonator sensor. Microwave and Telecommunication Technology (CriMiCo), 2012 22nd International Crimean Conference. Sevastopol, Crimea. 10-14.9.2012. pp. 853-854.
- Olkkonen, M.-K., Eskelinen, P., Huuskonen-Snicker, E., Pellinen, T., and Olmos Martinez, P. (2014). A New Microwave Asphalt Radar. RADAR 2014 (International Radar Conference 2014). Lille, France. 13-17.10.2014.
- Olkkonen, M.-K., Eskelinen, P., Huuskonen-Snicker, E., Pellinen, T., and Olmos Martinez, P. (2015). An evaluation of the permittivity of two different rock types using microwave resonator and waveguide cutoff principles. *Frequenz*. Vol. 69:1-2. pp. 75-82.
- Orlando, L., and Slob, E. (2009). Using multicomponent GPR to monitor cracks in a historical building. *Journal of Applied Geophysics*. Vol. 67:4. pp. 327-334.
- Pajewski, L., Benedetto, A., Derobert, X., Giannopoulos, A., Loizos, A., Manacorda, G., Marciniak, M., Plati, C., Schettini, G., and Trinks, I. (2013) Applications of Ground Penetrating Radar in civil engineering – COST action TU1208. Advanced Ground Penetrating Radar (IWAGPR), 2013 7th International Workshop on. Nantes. 2-5.7.2013.
- PANK-4122. (2008). Asfalttimassat ja -päällysteet, perusmenetelmät. Asfalttipäällysteen tyhjättila, päällystetutka-menetelmä. Päällystealan neuvottelukunta PANK ry. In Finnish.
- PANK ry. (2011). Asfalttinormit 2011. Päällystealan neuvottelukunta PANK ry. 118 p. ISBN 978-952-99985-1-7. In Finnish.
- Parkhomenko, E. I. (1967). Electrical Properties of Rocks. Keller, G. V. (ed.) New York: Plenum Press.
- Pellinen, T., Eskelinen, P., Huuskonen-Snicker, E., and Hartikainen, A. (2015a). Assessment of air void content of asphalt using dielectric constant measurements by GPR and with VNA. Espoo: Aalto University. Aalto University publication series SCIENCE + TECHNOLOGY, 9/2015. Available at: <http://urn.fi/URN:ISBN:978-952-60-6288-4>
- Pellinen, T., Huuskonen-Snicker, E., Eskelinen, P., and Olmos Martinez, P. (2015b). Representative volume element of asphalt pavement for electromagnetic measurements. *Journal of Traffic and Transportation Engineering (English Edition)*. Vol. 2:1. pp. 30-39.
- Pellinen, T., Eskelinen, P., Hartikainen, A. Huuskonen-Snicker, E., and Eskelinen, J. (2016). Assessment of air void content of asphalt using dielectric constant measurements by GPR and with microwave radar. Espoo: Aalto University. Aalto University publication series SCIENCE + TECHNOLOGY, 8/2016. Available at: <http://urn.fi/URN:ISBN:978-952-60-6879-4>

- Pinel, N., Le Bastard, C. and Bourlier, C. (2015). Asymptotic modelling of coherent scattering from rough pavements. Radar Conference (EuRAD), 2015 European. Paris, France. 9-11.9.2015. pp. 221-224.
- Plati, C., and Loizos, A. (2013). Estimation of in-situ density and moisture content in HMA pavements based on GPR trace reflection amplitude using different frequencies. *Journal of Applied Geophysics*. Vol. 97. pp. 3-10.
- Podd, F. J. W., Peyton, A. J., and Armitage, D. W. (2015). GPR combined with a positioning system to detect anti-personnel landmines. Advanced Ground Penetrating Radar (IWAGPR), 2015 8th International Workshop on. Florence, Italy. 7-10.7.2015. pp. 1-4.
- Poikajärvi, J., Peisa, K., Herronen, T., Aursand, P. O., Maijala, P., and Narbro, A. (2012). GPR in road investigations – equipment tests and quality assurance of new asphalt pavement. *Nondestructive Testing and Evaluation*. Vol. 27:3. pp. 293-303.
- Pokorný, J., Pokorný, P., Suza, P., and Hrouda, F. (2011). A multi-function Kappa-bridge for high precision measurement of the AMS and the variations of magnetic susceptibility with field, temperature and frequency. In: Petrovský, E., Herrero-Bervera, E., Harinarayana, T., Ivers, D. (eds.) *The Earth's Magnetic Interior*. Springer. pp 292-301. Volume 1 of the series IAGA Special Sopron Book Series.
- Presuel-Moreno, F. J., and Sagüés, A. A. (2009). Bulk magnetic susceptibility measurements for determination of fly ash presence in concrete. *Cement and Concrete Research*. Vol. 39:2. pp. 95-101.
- Puranen, R. (1989). Susceptibilities, iron and magnetite content of Precambrian rocks in Finland. Espoo: Geological Survey of Finland. Report of Investigation 90.
- Radzevicius, S. J., and Daniels, J. J. (2000). Ground penetrating radar polarization and scattering from cylinders. *Journal of Applied Geophysics*. Vol. 45:2. pp. 111-125.
- Ramo, S., Whinnery, J. (1956). *Fields and Waves in Modern Radio*. 2nd ed. New York: John Wiley & Sons.
- Roimela, P. (1998). Päälystetutkatutkimukset 1996-1997. Rovaniemi: Tielaitos. Tielaitoksen selvityksiä 4/1998. In Finnish.
- Räisänen, M. (2004). From outcrops to dust - mapping, testing, and quality assessment of aggregates. Doctoral thesis. University of Helsinki, Department of Geology. Helsinki.
- Räisänen, M., and Torppa, A. (2005). Quality assessment of a geologically heterogeneous rock quarry in Pirkanmaa county, southern Finland. *Bulletin of Engineering Geology and the Environment*. Vol. 64:4. pp. 409-418.
- Saarenketo, T. (1997). Using ground-penetrating radar and dielectric probe measurements in pavement density quality control. *Transportation Research Record*. Vol. 1575. pp. 34-41.
- Saarenketo, T. (1998). Electrical properties of water in clay and silty soils. *Journal of Applied Geophysics*. Vol. 40:1-3. pp. 73-88.
- Saarenketo, T., and Scullion, T. (2000). Road evaluation with ground penetrating radar. *Journal of Applied Geophysics*. Vol. 43:2-4. pp. 119-138.
- Saarenketo, T. (2006). Electrical properties of road materials and subgrade soils and the use of ground penetrating radar in traffic infrastructure surveys. Doctoral thesis. University of Oulu, Faculty of Science, Department of Geosciences. Oulu.
- Saarenketo, T. (2009). NDT Transportation. In: Jol, H. M. (ed.) *Ground Penetrating Radar Theory and Applications*. Amsterdam: Elsevier. pp. 395-444.

- Sarabandi, K., Li, E. S., and Nashashibi, A. (1997). Modeling and measurements of scattering from road surfaces at millimeter-wave frequencies. *IEEE Transactions on Antennas and Propagation*. Vol. 45:11. pp. 1679-1688.
- Sbartai, Z. M., Laurens, S., Rhazi, J., Balayssac, J. P., and Arliguie, G. (2007). Using radar direct wave for concrete condition assessment: Correlation with electrical resistivity. *Journal of Applied Geophysics*. Vol. 62:4. pp. 361-374.
- Scheer, J. (1983). Radar reflectivity calibration procedures. In: Currie, N. (ed.) *Techniques of radar reflectivity measurement*. Norwood, MA: Artech House. pp. 109-132.
- Schön, J. H. (1996). *Physical Properties of Rocks: Fundamentals and Principles of Petrophysics*. Oxford: Pergamon. 583 p. *Handbook of Geophysical Exploration: Seismic Exploration (Volume 18)*.
- Sebesta, S., Scullion, T., and Saarenketo, T. (2013). Using Infrared and High-Speed Ground-Penetrating Radar for Uniformity Measurements on New HMA Layers. Washington, D.C.: Transportation Research Board. 80 p. Report S2-R06C-RR-1.
- SFS-EN 1097-7. (2008). Tests for mechanical and physical properties of aggregates. Part 7: Determination of the particle density of filler. Pyknometer method. Helsinki: Finnish Standards Association SFS.
- SFS-EN 12697-5. (2012). Bituminous mixtures. Test methods for hot mix asphalt. Part 5: Determination of the maximum density. Helsinki: Finnish Standards Association SFS.
- SFS-EN 12697-6. (2012). Bituminous mixtures. Test methods for hot mix asphalt. Part 6: Determination of bulk density of bituminous specimens. Helsinki: Finnish Standards Association SFS.
- Shang, J., Umana, J., Bartlett, F., and Rossiter, J. (1999). Measurement of Complex Permittivity of Asphalt Pavement Materials. *Journal of Transportation Engineering*. Vol. 125:4. pp. 347-356.
- Shaw, M. R., Millard, S. G., Molyneaux, T. C. K., Taylor, M. J., and Bungey, J. H. (2005). Location of steel reinforcement in concrete using ground penetrating radar and neural networks. *NDT & E International*. Vol. 38:3. pp. 203-212.
- Shell Bitumen. (1990). *The Shell Bitumen handbook*. Chertsey: Shell Bitumen U.K. ISBN 0-9516625-0-3.
- Sihvola, A. H. (1989). Self-consistency aspects of dielectric mixing theories. *IEEE Transactions on Geoscience and Remote Sensing*. Vol. 27:4. pp. 403-415.
- Sihvola, A. (1999). *Electromagnetic mixing formulas and applications*. London: Institution of Electrical Engineers. 284 p.
- Siren, T., Kantia, P., and Rinne, M. (2015). Considerations and observations of stress-induced and construction-induced excavation damage zone in crystalline rock. *International Journal of Rock Mechanics and Mining Sciences*. Vol. 73. pp. 165-174.
- Soutsos, M. N., Bungey, J. H., Millard, S. G., Shaw, M. R. and Patterson, A. (2001). Dielectric properties of concrete and their influence on radar testing. *NDT & E International*. Vol. 34:6. pp. 419-425.
- Sun, M., Pinel, N., Le Bastard, C., Baltazart, V., Ihamouten, A., and Wang, Y. (2015). Time delay and interface roughness estimations by GPR for pavement survey. *Near Surface Geophysics*. Vol. 13:3. pp. 279-287.
- Takahashi, K., Preetz, H., and Igel, J. (2011). Soil properties and performance of landmine detection by metal detector and ground-penetrating radar — Soil characterisation and its verification by a field test. *Journal of Applied Geophysics*. Vol. 73:4. pp. 368-377.

- Tsui, F., and Matthews, S. L. (1997). Analytical modelling of the dielectric properties of concrete for subsurface radar applications. *Construction and Building Materials*. Vol. 11:3. pp. 149-161.
- Ulaby, F. T., Bengal, T. H., Dobson, M. C., East, J. R., Garvin, J. B., and Evans, D.L. (1990). Microwave dielectric properties of dry rocks. *IEEE Transactions on Geoscience and Remote Sensing*. Vol. 28:3. pp. 325-336.
- Van Dam, R. L., Hendrickx, J. M. H., Cassidy, N. J., North, R. E., Dogan, M., and Borchers, B. (2013). Effects of magnetite on high-frequency ground-penetrating radar. *Geophysics*. Vol. 78:5. H1-H11.
- Van Overmeeren, R. A. (1998). Radar facies of unconsolidated sediments in The Netherlands: A radar stratigraphy interpretation method for hydrogeology. *Journal of Applied Geophysics*. Vol. 40:1-3. pp. 1-18.
- Von Hippel, A. R. (1954). Dielectrics and waves. New York: John Wiley & Sons, Inc. 284 p.
- Yarovoy, A. G., Savelyev, T. G., Aubry, P. J., Lys, P. E., and Ligthart, L. P. (2007). UWB Array-Based Sensor for Near-Field Imaging. *IEEE Transactions on Microwave Theory and Techniques*. Vol. 55:6. pp. 1288-1295.
- Zhang, F., Xie, X., and Huang, H. (2010). Application of ground penetrating radar in grouting evaluation for shield tunnel construction. *Tunnelling and Underground Space Technology*. Vol. 25:2. P. 99-107.
- Zhao, S., and Al-Qadi, I. L. (2016). Development of an analytic approach utilizing the extended common midpoint method to estimate asphalt pavement thickness with 3-D ground-penetrating radar. *NDT & E International*. Vol. 78. pp. 29-36.





ISBN 978-952-60-7229-6 (printed)  
ISBN 978-952-60-7228-9 (pdf)  
ISSN-L 1799-4934  
ISSN 1799-4934 (printed)  
ISSN 1799-4942 (pdf)

**Aalto University**  
**School of Engineering**  
**Department of Civil Engineering**  
[www.aalto.fi](http://www.aalto.fi)

**BUSINESS +  
ECONOMY**

**ART +  
DESIGN +  
ARCHITECTURE**

**SCIENCE +  
TECHNOLOGY**

**CROSSOVER**

**DOCTORAL  
DISSERTATIONS**